Simulating Turduckened Black Holes with a Discontinuous Galerkin Scheme

Michael Wagman

Senior Honors Thesis for Mathematics-Physics ScB
Brown University Physics Department
Jan Hesthaven, Brown University Applied Math Department, Adviser

In this thesis we review how general relativity is reformulated to solve initial value problems and discuss in particular the GBSSN system, a variant of the traditional BSSN formulation commonly used in numerical relativity. We then construct a discontinuous Galerkin scheme for numerically solving the GBSSN system and describe how to incorporate the turduckening technique for smoothing singularities in initial data for black holes. We then present numerical simulations of a turduckened black hole in spherical symmetry that build on the dG scheme used in [23] to simulate black holes using excision, and we show that the robust stability and spectral convergence of these simulations is maintained when we incorporate the turduckening technique. A first order reduction of the GBSSN system is then presented along with the results of numerical simulations using both excision, found to be stable and spectrally convergent, and turduckening, found to be unstable with our present implementation. Finally, we present a dG scheme for evolving a massless scalar field coupled to the GBSSN system and discuss preliminary results showing the scheme allows for stable simulations of the coupled system, in particular the infall and absorption of a scalar field pulse by a black hole.

I. INTRODUCTION

General relativity, Einstein's theory of gravity in which massive objects distort the geometry of spacetime, has proven to be wildly successful at modeling a wide range of astrophysical phenomena. In the early twentieth century, general relativity (GR) gained prominence by explaining a well-known discrepancy between observation and Newtonian calculations for the precession of Mercury's orbit and famously predicting the correct deflection of starlight by the sun during a 1919 eclipse. Since then the quantitative accuracy of GR has been tested with precision (see [47] for a review) and a number of often surprising general phenomena predicted by the theory have been observed. Perhaps the most notable phenomenon is the existence of black holes, objects so dense that the paths of all light rays inside a surface surrounding the black hole called the event horizon are bent so that they must travel inwards towards the center of the black hole. Black holes are generically predicted to form when dense objects collapse under the pull of their own gravity, and there is a great deal of indirect observational evidence that astrophysical black holes do indeed exist, including supermassive black holes at the center of the Milky Way and other galaxies. See [7] for a history of black hole theory and observational evidence.

Direct tests of GR are often extremely difficult due to the weakness of gravity when compared to the fundamental forces of particle physics; in "natural" units gravity is 10^{42} times weaker than electromagnetism. One important phenomenon predicted by GR is the existence of gravitational waves, distortions in the curvature of spacetime and the distance between nearby points that propagate through space at a finite speed (in fact the speed of light) and obey the standard wave equation in the limit of weak gravitational coupling. By comparison Newtonian gravity couples all points in space at a fixed time–indeed the impossibility of reconciling this fact with the fundamental postulate of special relativity that information cannot travel faster then the speed of light already shows the need for a very different relativistic theory of gravity–and so Newtonian gravity does not allow for such gravitational disturbances propagating at finite speed. Indirect evidence for gravitational waves has been provided by observations of binary pulsar systems, and measurements of a decay in the orbital period of the Hulse Taylor Binary in agreement with the predicted energy loss from gravitational wave emissions led to a 1993 Nobel prize [33].

Direct detection and measurements of gravitational waves would constitute important evidence for this prediction and allow for precise tests of GR in the strongly coupled regime where detectable waves would be formed. Furthermore, because gravitational waves interact with matter so weakly, waves formed in the early universe may look very similar today to when they were emitted and the direct observation of gravitational waves may open useful new avenues for early-universe astronomy. Experiments have been designed to detect gravitational waves through interferometry, and a new generation of upgraded detectors, most notably Advanced LIGO and Advanced Virgo, will be operational by 2015 and should be sensitive enough to detect the gravitational waves emitted from the strongest predicted sources. Such sources should be very massive, not overly symmetric (in particular not axisymmetric) systems whose gravitational profile varies significantly in time. The prime example of such a source is a binary black hole system in which two nearby black holes collide through a process of three phases called inspiral, merger, and ringdown. The resulting black hole will have less energy then the original dynamic binary black hole system with the difference radiated away as gravitational waves. Highly accurate models of the gravitational waveforms that should be emitted by binary black hole systems and other strong sources

of gravitational waves are critical to successful experimental detection, as detectors rely on a process of matched filtering to separate potential signals from background noise. The current state of LIGO and Virgo and the quest for direct detection of gravitational waves is reviewed in [36].

Unfortunately there is no way to analytically calculate the details of a binary black hole collision. Apart from perturbative expansions useful only for weakly coupled systems, there are no straightforward techniques for solving the equations of general relativity for a generic system. To get highly accurate predictions of gravitational waveforms, we are therefore led to consider numerical simulations of binary black holes and other systems in general relativity. Such precise numerical simulations inevitably require costly computation, and gravitational wave detectors should ideally have a wide catalog of possible waveforms that can be compared to observed signals. It is therefore important to find a computationally efficient numerical scheme whose accuracy increases quickly with increased computational resolution.

Stable numerical simulations of binary black hole collisions have been successfully constructed; the current state-of-the-art is reviewed in [42]. There are two main formulations of GR that have been used in stable simulations: the generalized harmonic formulation and the much more commonly used Baumgarte-Shapiro-Shibata-Nakamura (BSSN) formulation. Stable simulations for solving the BSSN system of partial differential equations (PDEs) have by and large relied on finite difference schemes. Finite difference schemes provide a simple means of numerically approximating solutions to PDEs, but the numerical error in such a scheme only decreases with increasing spatial resolution as some power of the resolution. Recent work by Field, Hesthaven, Lau, and Mroue in [23] has proposed an alternative approach for solving the BSSN system with a discontinuous Galerkin (dG) scheme in which the solution is approximated by local interpolating polynomials defined on subdomains that cover the whole computational domain. A significant advantage of dG schemes is a property known as spectral accuracy; the numerical error in the simulation decreases exponentially with increasing resolution. This high order accuracy, as well as robust stability in the presence of shocks, make a dG scheme a competitive choice for performing binary black hole simulations.

The simulations in [23] and those presented here are both limited to the model problem of evolving a single black hole in spherical symmetry for simplicity and relative computational ease. In the simulations in [23], the interior of the black hole's event horizon is removed from the computational domain in order to avoid the singularity present at the center of the black hole using a technique called excision. Performing excision relies on knowing the precise location of the event horizon of each black hole at all times. This means that binary block hole simulations with excision must include a computationally intensive process of horizon tracking, and state-of-the-art finite difference codes for solving the BSSN system avoid using excision [42]. In this thesis we will describe a modification to the dG BSSN simulations of Field et. al. in which the singularity is left in the computational domain but smoothed out through a process known as turduckening [14, 15] and present results from numerical simulations with dG BSSN solver that use both excision and turduckening.

The structure of the thesis is as follows: Chapter II describes the basic ingredients of GR, derives the ADM equations for formulating initial value problems in GR, and presents a BSSN-type formulation called the Generalized BSSN (GBSSN) system that will be solved in our numerical simulations. Chapter III provides a detailed description of dG methods and describes the construction of a scheme for solving the GBSSN system. Chapter IV describes

the construction of black hole initial data and the turduckening technique, the final elements necessary for building our simulations. The remaining chapters describe the results of our numerical simulations. Chapter V describes numerical simulations of a static black hole using a second order dG scheme and turduckening. Chapter VI describes simulations of a first order reduction of the scheme using both excision and turduckening that have been recently published in [11]. Finally, chapter VII derives the equations for evolving a massless scalar field coupled to the GBSSN system and describes some preliminary dG simulations of a localized scalar field pulse falling into a black hole.

II. GENERAL RELATIVITY AND THE GBSSN EQUATIONS

This chapter begins with a brief overview of general relativity and the aspects of differential geometry essential for understanding the Einstein field equations. The remainder of the chapter is devoted to reformulating the field equations in order to solve initial value problems in GR. Section B introduces new variables that allow us to define a decomposition of spacetime into a foliation of space-like hypersurfaces, Section C derives the ADM equations that reformulate the field equations in accordance with this decomposition, and Section D describes the GBSSN system, a further reformulation of the ADM system better suited for numerical evolution. The GBSSN system presented in Eq. (44) and Eq. (45) provides the constraint and evolution equations used in the numerical simulations to follow.

A. General Relativity and Spacetime Covariance

In classical Newtonian physics, particles live in Euclidean 3-space with a single time parameter agreed on by all observers throughout space. The combined spacetime is therefore described by $\mathbb{R}^3 \times \mathbb{R}$. Gravity is modeled as a force between massive objects that causes their paths to deviate from straight lines, the inertial trajectory of all particles. The situation is very different in GR. Gravity distorts the structure of spacetime itself. Massive particles still travel along their inertial paths under the influence of gravity, but these paths themselves curve in response to gravity.

To make this all precise, GR is described in the language of differential geometry. Spacetime is only assumed to be an arbitrary 4-dimensional manifold M, a topological space that looks locally like flat space (more precisely, every point is contained in a neighborhood diffeomorphic to a neighborhood of $\mathbb{R}^4$) but that may have a very different topological and geometric character from that of Euclidean space $\mathbb{R}^4$. This manifold is equipped with a symmetric, non-degenerate inner product $\overline{g}(\cdot, \cdot)$ called the metric[1] that provides a way to measure the lengths and angles of vectors. M is called a pseudo-Riemannian manifold when equipped with such a metric. The metric can by thought of as a generalization of the reg-

[1] Important note on notation: the metric on M will be denoted by $\overline{g}$ and sometimes called the physical metric to differentiate it from a metric γ defined on spatial slices of spacetime and a related metric g. This final metric is the one that is actually taken as an evolved variable in the simulations that follow, so we give it the simpler notation g. This makes the notation in this section a bit more cumbersome, but will greatly streamline the notation in the remainder of the thesis. We adopt a $(-,+,+,+)$ metric convention throughout and will use geometrized units in which $c = G = 1$.

ular dot product in Euclidean space. Generalizing the idea of geometric tangent vectors to curves and surfaces in $\mathbb{R}^3$, vectors are defined as elements of a vector space T_pM called the tangent space that is constructed at every point $p \in M$. This tangent space can in fact be rigorously defined as the collection of tangent vectors to all possible smooth curves passing through $p \in M$, that is directional derivative operators acting in all directions [38]. Linear maps $\omega : T_pM \to \mathbb{R}$ from vectors to the real numbers are called covectors and are described as elements of the dual space T_p^*M. The metric $\overline{g}$ is a linear map $T_pM \otimes T_pM \to \mathbb{R}$, that is a bilinear map taking two vectors to the reals. It is called a rank (0,2) tensor, and we can define tensors of arbitrary rank (p,q) as maps from p covectors and q vectors to the real numbers. According to the principle of general covariance, all objects and equations in general relativity are constructed using tensors to provide them with a geometric meaning that does not depend on a particular observer's choice of coordinate frame.

Choose coordinates (x^0, x^1, x^2, x^3) on some neighborhood of $p \in M$, and define a coordinate basis for T_pM by taking the directional derivative along each coordinate axis as a basis vector. For simplicity of notation we write $\partial_0 \equiv \frac{\partial}{\partial x^0}$, and so this coordinate basis is written $\{\partial_0, \partial_1, \partial_2, \partial_3\}$. We will use index notation to describe vectors and covectors by their components in such a coordinate basis; for example we describe a vector v by $v^\mu = (v^0, v^1, v^2, v^3)^T$ and a covector ω by $\omega_\mu = (\omega_0, \omega_1, \omega_2, \omega_3)$.[2] We further adopt the Einstein summation convention in which all contractions, defined as repeated upper-lower index pairs, are summed over, for example $v^\mu \omega_\mu \equiv \sum_{\mu=0}^{3} v^\mu \omega_\mu$. A general tensor of rank (p, q) can be described by its components $T^{\mu_1 \mu_2 \ldots, \mu_p}_{\nu_1 \nu_2 \ldots, \nu_q}$. Though the actual components of a tensor depend on the particular choice of coordinates, equations relating tensors are covariant, that is they are independent of a particular choice of coordinates. The physical metric $\overline{g}$ is described by it's components $\overline{g}_{\mu\nu}$. We further define an inverse metric $\overline{g}^{\mu\nu}$ by $\overline{g}_{\mu\nu}\overline{g}^{\mu\rho} = \delta^\rho_\nu$ where δ^ν_μ is the Kronecker delta, defined to be 1 if $\mu = \nu$ and 0 otherwise. We can raise and lower indices using the metric and inverse metric, defining for example $v_\mu \equiv \overline{g}_{\mu\nu} v^\nu$.

Since derivatives like ∂_μ obviously depend on the choice of coordinates, we look to define a coordinate independent tensorial analog of the partial derivative called a covariant derivative. This covariant derivative is denoted by $\overline{\nabla}_\mu$ and defined in the cases of vectors and covectors by

$$\overline{\nabla}_\mu v^\nu \equiv \partial_\mu v^\nu + \overline{\Gamma}^{\nu}_{\ \mu\sigma} v^\sigma \tag{1a}$$

$$\overline{\nabla}_\mu \omega_\nu \equiv \partial_\mu \omega_\nu - \overline{\Gamma}^{\sigma}_{\ \mu\nu} \omega_\sigma, \tag{1b}$$

where the connection $\overline{\Gamma}^{\mu}_{\ \nu\lambda}$ is a (non-tensorial) set of functions defined by

$$\overline{\Gamma}^{\mu}_{\ \nu\lambda} \equiv \frac{1}{2}\overline{g}^{\mu\sigma}(\partial_\lambda \overline{g}_{\nu\sigma} + \partial_\nu \overline{g}_{\lambda\sigma} - \partial_\sigma \overline{g}_{\nu\lambda}). \tag{2}$$

The covariant derivatives for tensors of higher rank are defined simply by adding another contraction of the connection with each raised index and subtracting a contraction of the connection with each lower index. For a full discussion of manifolds, tensors, covariant derivatives, etc in the language of general relativity see [20, 45]; for a mathematical treatment in the language of differential geometry see [21, 37, 38, 44].

[2] Another important note on notation: Greek indices like μ and ν represent the four-dimensional spacetime coordinates and will be assumed to run from 0 to 3, while Latin indices like i, j, k represent the three-dimensional spatial coordinates only and will be assumed to run from 1 to 3.

The notion of curvature can be precisely defined on a (pseudo-Riemannian) manifold by constructing the Riemann curvature tensor $\overline{R}^{\mu}{}_{\nu\lambda\rho}$ as

$$\overline{R}^{\mu}{}_{\nu\lambda\rho} \equiv \partial_\lambda \overline{\Gamma}^{\mu}{}_{\nu\rho} - \partial_\rho \overline{\Gamma}^{\mu}{}_{\nu\lambda} + \overline{\Gamma}^{\mu}{}_{\sigma\lambda}\overline{\Gamma}^{\sigma}{}_{\nu\rho} - \overline{\Gamma}^{\mu}{}_{\sigma\rho}\overline{\Gamma}^{\sigma}{}_{\nu\rho}. \tag{3}$$

Geometrically, $\overline{R}^{\mu}{}_{\nu\lambda\rho}$ represents the change in the components of the coordinate vector ∂_ρ when it is parallel transported around an infinitesimal closed loop along in the plane of ∂_ν and ∂_λ. We further define two contractions of the Riemann tensor called the Ricci tensor $\overline{R}_{\mu\nu}$ and Ricci scalar $\overline{R}$ by

$$\overline{R}_{\mu\nu} \equiv \overline{R}^{\lambda}{}_{\mu\lambda\nu} \tag{4}$$

$$\overline{R} \equiv \overline{R}^{\mu}{}_{\mu} = \overline{g}^{\mu\nu}\overline{R}_{\mu\nu}. \tag{5}$$

A manifold is called flat if and only if the Riemann tensor vanishes everywhere. Euclidean space and the Minkowski space of special relativity are both flat since the metric in both spaces is constant, $\mathrm{diag}(1,1,1,1)$ for $\mathbb{R}^4$ and $\mathrm{diag}(-1,1,1,1)$ for Minkowski space. In curved spacetime it is no longer reasonable to postulate that the inertial path taken by particles in the absence of an external force is a straight line defined by $\partial_t^2 q(t,x) = 0$, as can be seen by imagining a particle constrained to move along a sphere. Instead we postulate that particles travel along geodesics, paths that minimize the spacetime distance ds, defined by $ds^2 \equiv \overline{g}_{\mu\nu}dx^\mu dx^\nu$, integrated along the path. Geodesics are equivalently paths that satisfy the covariant generalization of straight-line paths $\overline{\nabla}_\mu \frac{dq}{dx^\nu} = 0$. Furthermore, light (and other massless fields) travel along null geodesics, paths for which $ds^2 = 0$. No causal information can travel faster than this, so the speed at which particles propagate along null geodesics defines the maximum speed of causal information flow.

The physical content of GR is given by the postulate that massive particles travel along time-like geodesics (geodesics where propagation is slower than light) and a description of how these geodesics are modified by the presence of other massive particles. Since the geodesic equation can be written in terms of the components of the metric, this is equivalent to a statement of how the metric responds to the presence of mass. Such as statement is given by the Einstein field equations

$$\overline{G}_{\mu\nu} \equiv \overline{R}_{\mu\nu} - \frac{1}{2}\,\overline{R}\,\overline{g}_{\mu\nu} = 8\pi T_{\mu\nu}, \tag{6}$$

where $T_{\mu\nu}$ is called the stress-energy tensor and characterizes the energy and momentum of matter throughout spacetime. It is defined and computed for a simple scalar field in Chapter VII. Note that in this equation and throughout this thesis we work in geometrized units where $G = c = 1$.

The Einstein field equations above provide a system of 10 PDEs (the metric is symmetric, $\overline{g}_{\mu\nu} = \overline{g}_{\nu\mu}$, and so are $\overline{R}_{\mu\nu}$ and $T_{\mu\nu}$) for the physical metric components $\overline{g}_{\mu\nu}$ in which each PDE involves non-linear products of the metric and its derivatives. While solving complicated non-linear PDEs is not an easy task in general, there is an even more troubling feature of this system: spatial and time derivatives are mixed together in non-trivial combinations. This is a natural feature of GR since there is to be no distinction between space and time apart from the sign of the metric and so any covariant equations must combine space and time components equally. It contrasts sharply, however, with the notion of solving an initial value problem in which a system is described by a "snapshot" of its state at one point in

time and then evolved to determine its state at future times. This is exactly the kind of problem that numerical simulations are equipped to solve, and indeed the type of problem that must be defined in order to model the gravitational waves emitted by a system starting in a specified binary black hole configuration.

Before we can begin describing a numerical scheme for solving Einstein's equations, we will need to re-formulate them as a system that describes the time evolution of the evolved fields ($\overline{g}_{\mu\nu}$ above) in terms of only the current state of the system at that point in time. This necessarily requires that we distinguish between space and time, so we will now describe how to reformulate GR in a way that breaks spacetime covariance by singling out a time direction but still maintains the physical content and the coordinate independence of the theory.

B. Basic Elements of a Spacetime Decomposition

1. Lapse, Shift, and Spatial Metric

A fundamental assumption in GR is that spacetime is locally flat, as reflected in the idea that we can choose local coordinates x^μ mapping a neighborhood around any point to a neighborhood of $\mathbb{R}^4$. $\overline{g}_{\mu\nu}$ is assumed to have signature +2, and so by purely linear algebraic considerations (see for example [35]) we can find coordinates in which it has a simple diagonal form at any given point. In particular we can choose coordinates so that at any given point $\overline{g}_{\mu\nu} = \eta_{\mu\nu} \equiv \text{diag}(-1, 1, 1, 1)$, the Minkowski metric of special relativity. In these coordinates we can clearly distinguish the time coordinate x^0. We can therefore foliate this local path of spacetime by hypersurfaces Σ_t defined as level sets of the time coordinate $t \equiv x^0$. As level sets of a smooth function, these hypersurfaces will be 3-dimensional embedded submanifolds of spacetime [38] and can be endowed with a spatial metric γ_{ij} that acts on three-dimensional vectors tangent to the hypersurface and describes the intrinsic geometry of the slice. This construction is non-covariant and can only be prescribed locally, but we follow [40] in using it to build an intuition for the (tensorial) objects used to define a geometric decomposition of spacetime into space and time.

In order to describe the time evolution of the system we must relate the coordinate system $x^i(t)$ on Σ_t with the coordinate system $x^i(t + dt)$ on a surface Σ_{t+dt} an infinitesimal time dt in the future. To be precise, we look to choose $x^i(t + dt)$ so that a Eulerian observer [25], an observer whose worldline is orthogonal to Σ_t and so views events on the hypersurface as simultaneous, at a point $p_t \in \Sigma_t$ is described by the coordinates $x^i(d + dt)$ after moving in time to the point $p_{t+dt} \in \Sigma_{t+dt}$. In flat spacetime this is simple. The Eulerian observer will always move in the x^0 direction, and so defining a time vector $t^\mu = (1, 0, 0, 0)$, we may set this vector equal to the unit normal vector for the hypersurface, n^μ. Proper time will be equal to coordinate time, and the proper distance between the point $p_t \in \Sigma_t$ and an arbitrary point $q_{t+dt} \in \Sigma_{t+dt}$ will be $ds^2 = \eta_{\mu\nu} dx^\mu dx^\nu = -dt^2 + dx^i dx_i$. To begin generalizing this, we can define a scalar function $\alpha(t, x^i)$ called the "lapse" that specifies a general relationship between proper time and coordinate time by $d\tau \equiv \alpha dt$. In this case the time evolution vector connecting the points p_t and p_{t+dt} is given by $t^\mu = (1, 0, 0, 0) = \alpha n^\mu$. Fig. 1 shows this construction along with the general case in which the time evolution vector may not be parallel to the normal vector.

In this case we describe the motion parallel to the hypersurface during time evolution by a spacelike vector $\beta^\mu = (0, \beta^i)$ called the "shift" and defined by $t^\mu = \alpha n^\mu + \beta^\mu$. The spatial

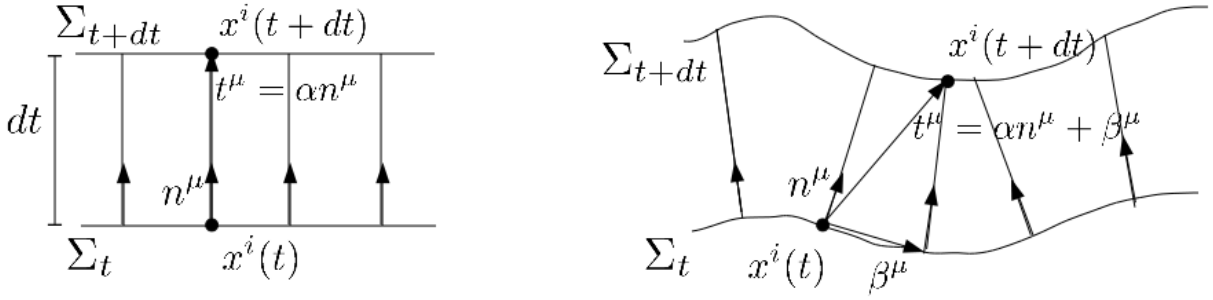

FIG. 1. Diagrams describing the relations between the lapse α, shift β, normal vector n^μ and time vector t^μ (note this time vector just gives the components of ∂_t). The left diagram represents flat space with coordinates chosen so that a Eulerian observer will measure zero spatial distance between $x^i(t)$ and $x^i(t+dt)$, and the right diagram describes a curved spatial slice where the Eulerian observer will measure a spatial shift between coordinates on the two slices.

distance between p_t and an arbitrary q_{t+dt} is then given by $dx^i + \beta^i dt$. In terms of α, β^i and the spatial metric γ_{ij} defined on Σ_t, the proper distance between arbitrary points on Σ_t and Σ_{t+dt} is given by

$$ds^2 = \overline{g}_{\mu\nu} dx^\mu dx^\mu = (-\alpha^2 + \gamma_{ij}\beta^i\beta^j)dt^2 + 2\gamma_{ij}\beta^i dt dx^j + \gamma_{ij} dx^i dx^j. \tag{7}$$

The components of the physical metric can immediately be read off from this equation, and inverting this 4x4 matrix gives the components of the inverse metric $\overline{g}^{\mu\nu}$. The metric and inverse metric are then given in block matrix form by

$$\overline{g}_{\mu\nu} = \begin{pmatrix} -\alpha^2 + \gamma_{ij}\beta^i\beta^j & \gamma_{ij}\beta^i \\ \gamma_{ij}\beta^j & \gamma_{ij} \end{pmatrix}, \qquad \overline{g}^{\mu\nu} = \begin{pmatrix} -1/\alpha^2 & \beta^j/\alpha^2 \\ \beta^i/\alpha^2 & \gamma^{ij} + \beta^i\beta^j/\alpha^2 \end{pmatrix}. \tag{8}$$

Since the physical metric $\overline{g}_{\mu\nu}$ is fundamental to the spacetime manifold and defined independently of the choice of foliation, Eq. (7) may be viewed as a definition of α, β, and γ_{ij} in terms of $\overline{g}_{\mu\nu}$. Furthermore, note that a choice of the fields $\alpha(t, x^i)$ and $\beta^i(t, x^i)$ just defines a relation between coordinate distance and proper distance. The lapse and shift are really gauge variables, and specifying a lapse and shift describes a particular choice of coordinates rather than specifying any physical information about the system. Also note that the expression $t^\mu = (1, 0, 0, 0) = \alpha n^\mu + \beta^\mu$ for the time vector provides an expression for the normal vector in these coordinates given by

$$n^\mu = \left(\frac{1}{\alpha}, -\frac{1}{\alpha}\beta^i\right). \tag{9}$$

Finally, a bit more must be said about the spatial metric γ. In Eq. (7) only the spatial components γ_{ij} appear, but it will prove useful to extend the spatial metric to a tensor $\gamma_{\mu\nu}$ that provides a map $T_pM \otimes T_pM \to \mathbb{R}$ rather than just $T_p\Sigma_t \otimes T_p\Sigma_t \to \mathbb{R}$. This four-dimensional spatial metric should still only describe spatial distances and should obviously agree with γ_{ij} for its spatial components. This can be accomplished by removing the lapse terms in $\overline{g}_{\mu\nu}$ that represent the time distance between slices but keeping the shift terms that

represent the spatial distance traveled as time progresses, and so we define

$$\gamma_{\mu\nu} \equiv \overline{g}_{\mu\nu} + n_\mu n_\nu = \begin{pmatrix} \gamma_{ij}\beta^i\beta^j & \gamma_{ij}\beta^i \\ \gamma_{ij}\beta^j & \gamma_{ij} \end{pmatrix}. \tag{10}$$

This tensor $\gamma_{\mu\nu}$ also provides us with a operator that projects 4-dimensional vectors onto the tangent space of each hypersurface $T_p\Sigma_t$, as may be verified in the case of an arbitrary vector u^ν:

$$\gamma^\nu_{\ \mu} u^\mu = \begin{pmatrix} 0 \\ u^1 + u^0\beta^1 \\ u^2 + u^0\beta^2 \\ u^3 + u^0\beta^3 \end{pmatrix}. \tag{11}$$

2. Intrinsic and Extrinsic Curvature

To finish describing our decomposition, we must be able to relate the curvature of Σ_t to the spacetime curvature described by $\overline{R}^\mu_{\ \nu\lambda\rho}$. We can define a notion of intrinsic curvature on Σ_t by building a connection $\tilde{\Gamma}^i_{jk}$ and a Riemann curvature tensor $\tilde{R}^i_{jk\ell}$ out of the spatial metric γ_{ij} since the hypersurface itself is a pseudo-Riemannian manifold. We can extend these to be four-dimensional tensors by constructing them from $\gamma_{\mu\nu}$. In analogy to Eqs. (2) and (3), we define

$$\tilde{\Gamma}^\mu_{\ \nu\lambda} \equiv \frac{1}{2}\gamma^{\mu\sigma}(\gamma_{\nu\sigma,\lambda} + \gamma_{\lambda\sigma,\nu} - \gamma_{\nu\lambda,\sigma}) \tag{12a}$$

$$\tilde{R}^\mu_{\ \nu\lambda\rho} \equiv \partial_\lambda \tilde{\Gamma}^\mu_{\ \nu\rho} - \partial_\rho \tilde{\Gamma}^\mu_{\ \nu\lambda} + \tilde{\Gamma}^\mu_{\ \sigma\lambda}\tilde{\Gamma}^\sigma_{\ \nu\rho} - \tilde{\Gamma}^\mu_{\ \sigma\rho}\tilde{\Gamma}^\sigma_{\ \nu\rho}. \tag{12b}$$

We can also build a covariant derivative operator D_μ using this connection in analogy to Eq. (1). This derivative operator can be verified to be the spatial projection of the spacetime covariant derivative, that is $D_\mu = \gamma^\nu_{\ \mu}\overline{\nabla}_\nu$. It can also be directly verified that any component of $\tilde{R}^\mu_{\ \nu\lambda\rho}$ with a 0 index will vanish, and so the spatial components of this tensor contain all the relevant information for the intrinsic curvature [40].

There is another notion of curvature called the "extrinsic curvature" of the submanifold. To get some geometric intuition, consider a 2-dimensional cylinder embedded in $\mathbb{R}^3$. Since a cylinder can be built by rolling up a flat piece of paper, it ought to have no intrinsic curvature. This is indeed the case; since constructing such a cylindrical space is equivalent to taking cylindrical coordinates for flat Euclidean space the Riemann tensor defined on the cylinder will vanish. Still, a cylinder in some sense "looks curved" when viewed in $\mathbb{R}^3$. It is this sense of curvature that is made precise by defining an extrinsic curvature tensor $K_{\mu\nu}$.

Consider an infinitesimal displacement dx^i along a hypersurface Σ_t. The normal vector $n^\mu(x^i + dx^i)$ will not in general be parallel to the normal vector $n^\mu(x^i)$, as is shown in Fig. 2, and the one-form dn^μ describing the difference between the two should be given by some linear function of dx^ν. These two one forms will naturally then be related by a rank (1,1) tensor $K^\mu_{\ \nu}$. We therefore define

$$K_{ij} \equiv -\overline{\nabla}_i n_j. \tag{13}$$

The extrinsic curvature tensor is symmetric, as will be verified shortly, and so we can replace $\nabla_i n_j$ with $\nabla_{(i} n_{j)} \equiv \frac{1}{2}(\nabla_i n_j + \nabla_j n_i)$ in the above definition. We wish the extrinsic curvature

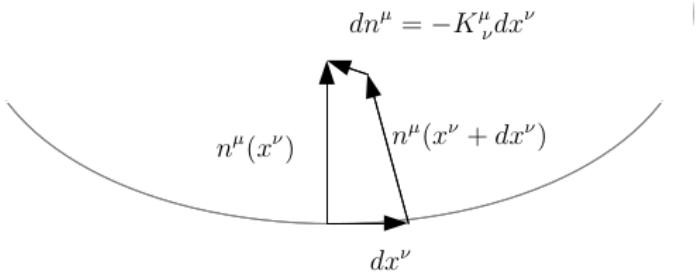

FIG. 2. The normal vector n^μ at points x^ν and $x^\nu + dx^\nu$ on a curved hypersurface Σ_t. By historical convention this surface is defined to have positive curvature. Since dn^μ points opposite to dx^ν in the diagram, we define $K_{\mu\nu}$ to have a negative sign in its definition to respect this convention.

to be purely spatial, so we can define a four-dimensional tensor $K_{\mu\nu}$ by taking a spatial projection of the four-dimensional analog of this definition,

$$K_{\mu\nu} \equiv -\gamma^\lambda_{\ \mu}\gamma^\rho_{\ \nu}\overline{\nabla}_{(\lambda}\, n_{\rho)}. \tag{14}$$

An equivalent and more computationally useful definition can be given in terms of a Lie derivative of the spatial metric. The Lie derivative is a derivative operator that has an elegant definition for an arbitrary manifold without reference to a metric in terms of the theory of flows along vector fields. For our purposes it can just be taken as a convenient shorthand for the combination of derivatives shown below, but it should be noted that all the connection terms in its definition cancel and so any of ∂_μ, $\overline{\nabla}_\mu$, or D_μ could equally well be used to take the Lie derivative. The definition of $K_{\mu\nu}$ as a Lie derivative is seen to be

$$\begin{aligned} -\frac{1}{2}\mathcal{L}_{\mathbf{n}}\gamma_{\mu\nu} &\equiv -\frac{1}{2}\left(n^\lambda D_\lambda \gamma_{\mu\nu} + \gamma_{\mu\lambda}D_\nu n^\lambda + \gamma_{\lambda\nu}D_\mu n^\lambda\right) \\ &= -\frac{1}{2}\left(0 + \gamma_{\mu\lambda}\gamma^\sigma_{\ \nu}\overline{g}^{\lambda\rho}\overline{\nabla}_\sigma n_\rho + \gamma_{\nu\lambda}\gamma^\sigma_{\ \mu}\overline{g}^{\lambda\rho}\overline{\nabla}_\sigma n_\rho\right) \\ &= -\frac{1}{2}\gamma^\rho_{\ \mu}\gamma^\sigma_{\ \nu}\left(\overline{\nabla}_\sigma n_\rho + \overline{\nabla}_\rho n_\sigma\right) = K_{\mu\nu}. \end{aligned} \tag{15}$$

C. The ADM Formalism

The first reformulation of the Einstein field equations suitable for solving general initial value problems was provided by Arnowitt, Deser, and Misner in 1959 by deriving what are now called the ADM equations [4]. These provide evolution equations for the spatial metric and extrinsic curvature as well as two constraint equations, purely spatial equations that must be satisfied on each hypersurface in the foliation. The structure of the equations is such that so long as the constraint equations are satisfied by the initial data specified on a spatial surface at the initial time $t = 0$ they will be preserved by the evolution equations and automatically satisfied at later times. We present a derivation of the ADM equations very different from the original and initially follow the approach of [40] before adopting the more abstract and fully covariant techniques of [9].

The ADM equations can be derived by combining the Einstein field equations with three equations that relate the the extrinsic and intrinsic curvature of the hypersurfaces to the spacetime curvature: the Gauss, Codazzi, and Ricci equations. The spatial pieces of the Gauss and Codazzi equations can be most easily derived by taking an orthogonal basis for our tangent space rather then the usual coordinate basis, so we will very briefly slip out of index notation and view for example the extrinsic curvature tensor $K(\cdot,\cdot)$ as an operator taking two vectors as inputs.

Let $\mathbf{f}_i$ be an orthonormal frame providing a basis for $T_p\Sigma_t$, and let $\mathbf{e}_i = (0, \mathbf{f}_i)$. Our normal vector $\mathbf{n}$ is orthogonal to the $\mathbf{e}_i$, so take $\{\mathbf{n}, \mathbf{e}_i\}$ as an orthogonal frame providing a basis for T_pM. Note that n^μ is normalized so that $\overline{g}(\mathbf{n},\mathbf{n}) = -1$. We mentioned upon defining the Riemann curvature tensor $\overline{R}^{\mu}{}_{\nu\lambda\rho}$ that it could be interpreted as measuring the change resulting from parallel transporting a vector around an infinitesimal closed loop. This is made precise in an equivalent definition of the Riemann curvature tensor as

$$\overline{R}\left(\mathbf{e}_i, \mathbf{e}_j, \mathbf{e}_k\right) = \overline{\nabla}_{\mathbf{e}_j}\overline{\nabla}_{\mathbf{e}_k}\mathbf{e}_i - \overline{\nabla}_{\mathbf{e}_k}\overline{\nabla}_{\mathbf{e}_j}\mathbf{e}_i \equiv \overline{\nabla}_j\overline{\nabla}_k\mathbf{e}_i - \overline{\nabla}_k\overline{\nabla}_j\mathbf{e}_i. \tag{16}$$

The components of this resultant vector will give $\overline{R}^{\mu}_{ijk}$ in terms of objects defined on the hypersurface as we desire, so we look to resolve the components of $\overline{\nabla}_k\mathbf{e}_i$ in the $\{\mathbf{n}, \mathbf{e}_i\}$ basis.

To calculate the spatial components, note that by the orthogonality of $\mathbf{e}_i$ and $\mathbf{e}_j$ we have $\partial_j\mathbf{e}_i = 0$, and so $\overline{\nabla}_k\mathbf{e}_i = \Gamma^{\ell}{}_{ik}\mathbf{e}_\ell$. This allows us to calculate the spatial components as

$$\overline{g}(\mathbf{e}_j, \overline{\nabla}_k\mathbf{e}_i) = \Gamma^{\ell}{}_{jk}\overline{g}\left(\mathbf{e}_\ell, \mathbf{e}_i\right) = \Gamma^{\ell}{}_{jk}\overline{g}_{\ell i} = \Gamma_{ijk}. \tag{17}$$

The 0 (normal) component is given by

$$\overline{g}(\mathbf{n}, \overline{\nabla}_k\mathbf{e}_i) = -\overline{g}(\mathbf{e}_i, \overline{\nabla}_k\mathbf{n}) = \overline{g}(\mathbf{e}_i, \mathbf{e}_j)K^j{}_k = \overline{g}_{ij}K^j{}_k = K_{ik}, \tag{18}$$

where the first equality follows from the orthogonality of $\mathbf{e}_i$ and $\mathbf{n}$ and the important property $\overline{\nabla}_\lambda\overline{g}_{\mu\nu} = 0$ called metric compatibility, as $0 = \overline{\nabla}_k\overline{g}\left(\mathbf{e}_i, \mathbf{n}\right) = \overline{g}\left(\overline{\nabla}_k\mathbf{e}_i, \mathbf{n}\right) + \overline{g}\left(\overline{\nabla}_k\mathbf{n}, \mathbf{e}_i\right)$. At this point we can easily verify that K_{ij} is symmetric as was asserted before:

$$K_{ji} = \overline{g}(\mathbf{n}, \overline{\nabla}_j\mathbf{e}_i) = \overline{g}(\mathbf{n}, \mathbf{e}_\mu)\Gamma^{\mu}{}_{ij} = \overline{g}(\mathbf{n}, \mathbf{e}_\mu)\Gamma^{\mu}{}_{ji} = \overline{g}(\mathbf{n}, \overline{\nabla}_i\mathbf{e}_j) = K_{ij}. \tag{19}$$

We can now express $\overline{\nabla}_k\mathbf{e}_i$ in terms of the $(\mathbf{n}, \mathbf{e}_i)$ basis by

$$\begin{aligned}\overline{\nabla}_k\mathbf{e}_i &= \overline{g}\left(\mathbf{n}, \overline{\nabla}_k\mathbf{e}_i\right)\frac{\mathbf{n}}{\overline{g}(\mathbf{n}\cdot\mathbf{n})} + \overline{g}\left(\mathbf{e}_j, \overline{\nabla}_k\mathbf{e}_i\right)\frac{\mathbf{e}_j}{\overline{g}(\mathbf{e}_j, \mathbf{e}_j)} \\ &= -K_{ik}\mathbf{n} + \Gamma^{\ell}{}_{ik}\mathbf{e}_\ell.\end{aligned} \tag{20}$$

Applying a second covariant derivative operator gives

$$\overline{\nabla}_j\overline{\nabla}_k\mathbf{e}_i = \overline{\nabla}_j\left(-K_{ik}\mathbf{n} + \Gamma^{\ell}{}_{ik}\mathbf{e}_\ell\right) = -\overline{\nabla}_jK_{ik}\mathbf{n} + \left(-K_{ik}K^\ell_j + \overline{\nabla}_j\Gamma^{\ell}{}_{ik} + \Gamma^m_{ik}\Gamma^{\ell}{}_{mj}\right)\mathbf{e}_\ell. \tag{21}$$

The second term of Eq. (16) is identical under an interchange of j and k, so we can now express the spacetime Riemann curvature tensor in terms of the extrinsic curvature and the intrinsic Riemann curvature tensor on the hypersurface as

$$\overline{R}\left(\mathbf{e}_i, \mathbf{e}_j, \mathbf{e}_k\right) = \left(\overline{\nabla}_kK_{ij} - \overline{\nabla}_jK_{ik}\right)\mathbf{n} + \left(K_{ij}K^\ell_k - K_{ik}K^\ell_j + \tilde{R}^{\ell}{}_{ijk}\right)\mathbf{e}_\ell. \tag{22}$$

The spatial piece of this equation decomposes the spatial curvature of the hypersurface into intrinsic and extrinsic parts and is known as Gauss's equation,

$$\overline{R}^{\ell}{}_{ijk} = \tilde{R}^{\ell}{}_{ijk} + K_{ik}K^{\ell}_{j} - K_{ij}K^{\ell}_{k}, \tag{23}$$

while the normal component describes how the extrinsic curvature changes throughout the foliation and is known as Codazzi's equation,

$$\overline{R}^{0}{}_{ijk} = \overline{\nabla}_k K_{ij} - \overline{\nabla}_j K_{ik}. \tag{24}$$

Rather than expressing these as spatial and normal components of the spacetime Riemann curvature tensor, we can write them as projections of the full tensor onto the spatial and normal directions. Gauss's equation is equivalent to

$$\gamma^{\lambda}_{\mu}\gamma^{\delta}_{\nu}\gamma^{\eta}_{\sigma}\gamma^{\xi}_{\rho}\overline{R}_{\lambda\delta\eta\xi} = \tilde{R}_{\mu\nu\sigma\rho} + K_{\nu\rho}K_{\mu\sigma} - K_{\nu\sigma}K_{\mu\rho}, \tag{25}$$

and Codazzi's equation can be expressed as

$$\gamma^{\eta}_{\nu}\gamma^{\rho}_{\sigma}\gamma^{\xi}_{\mu}n^{\lambda}\overline{R}_{\eta\rho\xi\lambda} = D_{\sigma}K_{\mu\nu} - D_{\nu}K_{\mu\sigma}. \tag{26}$$

The geometric structure of these equations as different projections of the Riemann curvature tensor is clear. The symmetries of the Riemann tensor dictate that projecting all four components onto the normal direction will trivially vanish, but there is one further non-trivial relation that can be found by projecting two components of $\overline{R}_{\mu\nu\lambda\sigma}$ onto the hypersurface and two onto the normal direction. This relation is known as the Ricci equation, and is given by [9]

$$\gamma^{\delta}_{\mu}\gamma^{\eta}_{\nu}n^{\sigma}n^{\lambda}\overline{R}_{\eta\sigma\delta\lambda} = \frac{1}{\alpha}D_{\mu}D_{\nu}\alpha + K^{\rho}_{\nu}K_{\mu\rho} + \mathcal{L}_{\mathbf{n}}K_{\mu\nu}. \tag{27}$$

The ADM constraint equations can be immediately derived from the Gauss and Codazzi equations as they are expressed above. Contracting the left side of Gauss's equation with $\gamma^{\mu\sigma}\gamma^{\nu\rho}$ and performing a series of index manipulations gives $2n^{\mu}n^{\nu}\overline{G}_{\mu\nu}$. This can be related to the stress-energy tensor by the Einstein field equations. To express the constraint concisely we define an energy density ρ by

$$\rho \equiv n^{\mu}n^{\nu}T_{\mu\nu}. \tag{28}$$

This has the physical interpretation of the energy density on the hypersurface as measured by a Eulerian observer. Combining the contracted form of Gauss's equation with the Einstein field equations provides the Hamiltonian constraint

$$\mathcal{H} \equiv \tilde{R} + K^2 - K_{ij}K^{ij} = 16\pi\rho. \tag{29}$$

Contracting the left side of Codazzi's equation with the spatial metric $\gamma^{\nu\sigma}$ can be shown to give $-\gamma^{\delta}_{\mu}n^{\lambda}\overline{R}_{\delta\lambda}$. Observing $\gamma^{\delta}_{\mu}n^{\lambda}\overline{g}_{\delta\lambda} = n_{\mu} - n_{\mu} = 0$, we can trivially add a term proportional to $\overline{g}_{\delta\lambda}$ and in particular can add $\frac{1}{2}\overline{R}\gamma^{\delta}_{\mu}n^{\lambda}\overline{g}_{\delta\lambda}$ so that this becomes a contraction of the Einstein tensor $\overline{G}_{\delta\lambda}$. For convenience we define this same contraction of the stress-energy tensor by

$$j_{\mu} \equiv -\gamma^{\delta}_{\mu}n^{\lambda}T_{\delta\lambda}. \tag{30}$$

j_{μ} can be interpreted as the momentum density measured by a Eulerian observer. Combining the Einstein field equations and the contracted Codazzi equation provides the momentum constraint

$$\mathcal{M}_i \equiv D_j K^{j}_{i} - D_i K = 8\pi j_i. \tag{31}$$

The remaining ADM equations are evolution equations for the spatial metric γ_{ij} and extrinsic curvature K_{ij}. Recall the definition of the time vector $t^\mu = \alpha n^\mu + \beta^\mu$ that has components $t^\mu = (1, 0, 0, 0)$ in our coordinate basis. Since any x^0 components of the spatial connection $\tilde{\Gamma}^\mu_{\nu\rho}$ will vanish, the Lie derivative along t^μ reduces to simply the partial derivative ∂_t in our chosen coordinates. The Lie derivative can itself be thought of a linear operator taking a vector and a tensor as input, and so $\mathcal{L}_{\mathbf{t}} = \alpha\mathcal{L}_{\mathbf{n}} - \mathcal{L}_{\boldsymbol{\beta}}$ [38].

The evolution equation for γ_{ij} can therefore be found immediately by rearranging Eq. (15) to give

$$\partial_t \gamma_{ij} = -2\alpha K_{ij} - \mathcal{L}_{\boldsymbol{\beta}}\gamma_{ij}. \tag{32}$$

The evolution equation for $K_{\mu\nu}$ can be found by rearranging the Ricci equation to solve for $\mathcal{L}_{\mathbf{n}}K_{\mu\nu}$ and decomposing this Lie derivative as above to give [9]

$$\partial_t K_{ij} = -D_i D_j \alpha - \alpha\left(\tilde{R}_{ij} - 2K_{ik}K^k_{\ j} + KK_{ij}\right) - 8\pi\alpha\left(S_{ij} - \frac{1}{2}\gamma_{ij}(S-\rho)\right) + \mathcal{L}_{\boldsymbol{\beta}}K_{ij}, \tag{33}$$

where we have introduced a spatial projection of the stress energy tensor

$$S_{\mu\nu} \equiv \gamma^\lambda_{\ \mu}\gamma^\rho_{\ \nu}T_{\lambda\rho}, \tag{34}$$

as well as the trace of this projection

$$S \equiv \gamma^{\mu\nu}S_{\mu\nu} = \gamma^{ij}S_{ij}. \tag{35}$$

We finally define the trace-free part of this tensor by

$$S^{\rm TF}_{ij} \equiv S_{ij} - \frac{1}{3}\gamma_{ij}S. \tag{36}$$

This will be featured in the next section.

D. The GBSSN System

The ADM evolution equations turn out to be poorly suited for numerical evolution[3]. Since the development of the ADM formalism, there have been numerous new formulations proposed in an effort to find a system more suitable for numerical evolution. The most popular in modern numerical relativity simulations are the generalized harmonic system and the BSSN system. There is even a range of systems described as BSSN-type formulations, see for example [8, 10, 12]. Our particular choice is commonly called the generalized BSSN or GBSSN formulation, and differs from the traditional BSSN formulation by defining all of the evolved fields to be tensors (except for one non-tensorial field related to the connection) rather than having some be objects known as tensor densities whose components pick up a weighted Jacobian factor when transformed to new coordinates. This is accomplished by removing the restriction present in traditional BSSN that the evolved metric to has unit determinant, consequently making the reduction to spherical symmetry, where in flat space

[3] More precisely they are only weakly hyperbolic when written in first order form [22], a condition that causes many numerical schemes to become unstable or lose convergence [17].

the spatial metric has determinant r^2, much simpler with GBSSN than with traditional BSSN.

We begin by defining a conformal spatial metric g_{ij} and a conformal factor χ by

$$g_{ij} \equiv \chi \gamma_{ij}, \qquad g^{ij} \equiv \frac{\gamma^{ij}}{\chi} \tag{37}$$

The conformal factor χ is a scalar that effectively rescales the spatial metric and is useful at least in spherical symmetry in isolating the divergences in the physical metric found at the central singularity of a black hole from the evolved conformal metric. When the spatial metric γ_{ij} diverges, we can allow the conformal metric g_{ij} to remain finite so long as the conformal factor χ approaches zero. It is similarly useful to perform this same conformal decomposition with the extrinsic curvature. Define the trace K and trace-free part A_{ij} of the conformal extrinsic curvature by

$$K_{ij} = \frac{1}{\chi}\left(A_{ij} + \frac{1}{3} g_{ij} K\right). \tag{38}$$

The trace K and trace-free part A_{ij} are evolved separately as independent fields. Also define a connection built from conformal spatial metric g_{ij} by

$$\Gamma^i_{jk} \equiv \frac{1}{2} g^{im}(\partial_k g_{mj} + \partial_j g_{mk} - \partial_m g_{jk}). \tag{39}$$

Finally define conformal connection functions by contracting the conformal connection with the spatial metric,

$$\Gamma^i \equiv g^{jk}\Gamma^i_{jk} = -\frac{1}{\sqrt{g}}\partial_j\left(\sqrt{g} g^{ij}\right). \tag{40}$$

These conformal connection functions provide the final evolved variables for the GBSSN system. The full set of evolved variables in GBSSN are then the gauge variables α, β^i, and B^i, a vector to be introduced shortly in the evolution equations that introduces damping to the shift vector, and the physical fields g_{ij}, A_{ij}, K, Γ^i, and χ.

Evolution equations for the gauge variables may be chosen freely, but the numerical stability of the resulting scheme depends greatly on this choice. We use the "1+log" and "Γ-driver" conditions [1] common to nearly all stable binary black hole evolutions using BSSN [42]. As can be seen from Eq. (37), there is also some ambiguity in determining the evolution equations for both the conformal factor and the conformal metric from the ADM evolution equation for the spatial metric. This ambiguity and a similar ambiguity resulting from conformal decomposition of the extrinsic curvature are resolved by explicitly specifying the evolution of the conformal metric determinant g. This provides the major distinction between traditional BSSN formulations alluded to earlier: in traditional BSSN $g = 1$ for all times, while we specify a "Lagrangian condition" $\partial_t(\ln g) = 0$ [12].

All of the numerical simulations presented in this thesis are limited to spherically symmetric spacetimes, so we will immediately specialize to this case. The spherically symmetric line element is given in terms of the evolved GBSSN variables by

$$ds^2 = \left(-\alpha^2 + \frac{\beta^{r2} g_{rr}}{\chi}\right) dt^2 + \frac{2\beta^r g_{rr}}{\chi} dt dr + \frac{g_{rr}}{\chi} dr^2 + \frac{g_{\theta\theta}}{\chi}(d\theta^2 + \sin^2\theta d\phi^2). \tag{41}$$

Note that in these coordinates radially incoming and outgoing null geodesics, defined as paths satisfying $ds^2 = 0$, have coordinate velocity

$$\frac{dr}{dt} = -\beta^r \pm \alpha\sqrt{\frac{\chi}{g_{rr}}}. \tag{42}$$

Subject to spherical symmetry, the conformal connection and trace-free conformal extrinsic curvature reduce to [23]

$$\Gamma^i = \begin{pmatrix} \Gamma^r \\ -\frac{\cos\theta}{g_{\theta\theta}\sin\theta} \\ 0 \end{pmatrix}, \qquad A_{ij} = A_{rr}\begin{pmatrix} 1 & 0 & 0 \\ 0 & -\frac{g_{\theta\theta}}{2g_{rr}} & 0 \\ 0 & 0 & -\frac{g_{\theta\theta}\sin^2\theta}{2g_{rr}} \end{pmatrix}. \tag{43}$$

This means that in spherical symmetry our evolved fields are just α, β^r, B^r, g_{rr}, $g_{\theta\theta}$, A_{rr}, K, Γ^r, and χ.

A full derivation of the spherically symmetric GBSSN evolution and constraint equations from the ADM equations is presented in Appendix A of [22] using the choices described above for the evolution of the gauge variables and conformal metric determinant in notation identical to that of this thesis except that conformal variables have bars instead of physical variables, so we will not repeat the calculation here. Using the ADM evolution equations and the choices described above, the GBSSN evolution equations in spherical symmetry are given by

$$\partial_t\alpha = \beta^r\alpha' - 2\alpha K - (\partial_t\alpha)_0 \tag{44a}$$

$$\partial_t\beta^r = \beta^r\beta^{r\prime} + \frac{3}{4}B^r - (\partial_t\beta^r)_0 \tag{44b}$$

$$\partial_t B^r = \beta^r B^{r\prime} + \lambda(\partial_t\Gamma^r - \beta^r\Gamma^{r\prime}) - \eta B^r - (\partial_t B^r)_0 \tag{44c}$$

$$\partial_t\chi = \beta^r\chi' + \frac{2}{3}K\alpha\chi - \frac{\beta^r g'_{rr}\chi}{3g_{rr}} - \frac{2\beta^r g'_{\theta\theta}\chi}{3g_{\theta\theta}} - \frac{2}{3}\beta^{r\prime}\chi \tag{44d}$$

$$\partial_t g_{rr} = \frac{2}{3}\beta^r g'_{rr} + \frac{4}{3}g_{rr}\beta^{r\prime} - 2A_{rr}\alpha - \frac{2g_{rr}\beta^r g'_{\theta\theta}}{3g_{\theta\theta}} \tag{44e}$$

$$\partial_t g_{\theta\theta} = \frac{1}{3}\beta^r g'_{\theta\theta} + \frac{A_{rr}g_{\theta\theta}\alpha}{g_{rr}} - \frac{g_{\theta\theta}\beta^r g'_{rr}}{3g_{rr}} - \frac{2}{3}g_{\theta\theta}\beta^{r\prime} \tag{44f}$$

$$\begin{aligned}\partial_t A_{rr} = {} & \beta^r A'_{rr} + \frac{4}{3}A_{rr}\beta^{r\prime} - \frac{\beta^r g'_{rr}A_{rr}}{3g_{rr}} - \frac{2\beta^r g'_{\theta\theta}A_{rr}}{3g_{\theta\theta}} + \frac{2\alpha\chi(g'_{rr})^2}{3g_{rr}^2} - \frac{\alpha\chi(g'_{\theta\theta})^2}{3g_{\theta\theta}^2} \\ & - \frac{\alpha(\chi')^2}{6\chi} + \frac{2}{3}g_{rr}\alpha\chi\Gamma^{r\prime} - \frac{\alpha\chi g'_{rr}g'_{\theta\theta}}{2g_{rr}g_{\theta\theta}} + \frac{\chi g'_{rr}\alpha'}{3g_{rr}} + \frac{\chi g'_{\theta\theta}\alpha'}{3g_{\theta\theta}} - \frac{\alpha g'_{rr}\chi'}{6g_{rr}} - \frac{\alpha g'_{\theta\theta}\chi'}{6g_{\theta\theta}} \\ & - \frac{2}{3}\alpha'\chi' + \frac{\alpha\chi''}{3} - \frac{2}{3}\chi\alpha'' - \frac{\alpha\chi g''_{rr}}{3g_{rr}} + \frac{\alpha\chi g''_{\theta\theta}}{3g_{\theta\theta}} - \frac{2\alpha A_{rr}^2}{g_{rr}} + K\alpha A_{rr} - \frac{2g_{rr}\alpha\chi}{3g_{\theta\theta}} \\ & - 8\pi\alpha\chi S_{rr}^{\mathrm{TF}}\end{aligned} \tag{44g}$$

$$\partial_t K = \beta^r K' + \frac{\chi g'_{rr}\alpha'}{2g_{rr}^2} - \frac{\chi g'_{\theta\theta}\alpha'}{g_{rr}g_{\theta\theta}} + \frac{\alpha'\chi'}{2g_{rr}} - \frac{\chi\alpha''}{g_{rr}} + \frac{3\alpha A_{rr}^2}{2g_{rr}^2} + \frac{1}{3}\alpha K^2 + 4\pi\alpha(S+\rho) \tag{44h}$$

$$\begin{aligned}\partial_t\Gamma^r = {} & \beta^r\Gamma^{r\prime} + \frac{A_{rr}\alpha g'_{\theta\theta}}{g_{rr}^2 g_{\theta\theta}} + \frac{2\beta^{r\prime}g'_{\theta\theta}}{3g_{rr}g_{\theta\theta}} + \frac{A_{rr}\alpha g'_{rr}}{g_{rr}^3} - \frac{4\alpha K'}{3g_{rr}} - \frac{2A_{rr}\alpha'}{g_{rr}^2} - \frac{3A_{rr}\alpha\chi'}{g_{rr}^2\chi} \\ & + \frac{4\beta^{r\prime\prime}}{3g_{rr}} - \frac{\beta^r(g'_{\theta\theta})^2}{g_{rr}g_{\theta\theta}^2} + \frac{\beta^r g''_{rr}}{6g_{rr}^2} + \frac{\beta^r g''_{\theta\theta}}{3g_{\theta\theta}g_{rr}} - \frac{16\pi\alpha j^r}{\chi},\end{aligned} \tag{44i}$$

where primes denote spatial derivatives and a few new parameters have been introduced that need to be defined. η is a constant that damps the field B^r featured in the evolution of the shift β^r and is chosen for numerical stability. λ is another constant chosen for numerical stability. It affects the speed at which information propagates in the gauge sector and the coordinate location past which no information about the evolved fields can escape a black hole, as will be discussed in the next chapter. Finally $(\partial_t \alpha)_0$, $(\partial_t \beta^r)_0$ and $(\partial_t B^r)_0$ are modifications to the usual 1+log and Γ-driver conditions. They are defined to be the values of $\partial_t \alpha$, $\partial_t \beta$, and $\partial_t B^r$ at $t = 0$ respectively and force the gauge variables to be static at the initial time.

There is one new set of constraint equations introduced in BSSN formulations by the definition of the conformal connection functions: $\mathcal{G}^i \equiv \Gamma^i - g^{jk}\Gamma^i_{jk} = 0$. The full set of GBSSN constraint equations in spherical symmetry is given by

$$\begin{aligned}\mathcal{H} = 16\pi\rho = &-\frac{3A_{rr}^2}{2g_{rr}^2} + \frac{2K^2}{3} - \frac{5(\chi')^2}{2\chi g_{rr}} + \frac{2\chi''}{g_{rr}} + \frac{2\chi}{g_{\theta\theta}} \\ &- \frac{2\chi g''_{\theta\theta}}{g_{rr}g_{\theta\theta}} + \frac{2\chi' g'_{\theta\theta}}{g_{rr}g_{\theta\theta}} + \frac{\chi g'_{rr}g'_{\theta\theta}}{g_{rr}^2 g_{\theta\theta}} - \frac{\chi' g'_{rr}}{g_{rr}^2} + \frac{\chi (g'_{\theta\theta})^2}{2g_{rr}g_{\theta\theta}^2} \end{aligned} \tag{45a}$$

$$\mathcal{M}_r = 8\pi j_r = \frac{A'_{rr}}{g_{rr}} - \frac{2K'}{3} - \frac{3A_{rr}\chi'}{2\chi g_{rr}} + \frac{3A_{rr}\chi'}{2\chi g_{rr}} + \frac{3A_{rr}g'_{\theta\theta}}{2g_{rr}g_{\theta\theta}} - \frac{A_{rr}g'_{rr}}{g_{rr}^2} \tag{45b}$$

$$\mathcal{G}^r = 0 = -\frac{g'_{rr}}{2g_{rr}^2} + \frac{g'_{\theta\theta}}{g_{rr}g_{\theta\theta}} + \Gamma^r. \tag{45c}$$

After specifying initial data for a particular system in terms of the evolved GBSSN variables, our numerical simulations are carried out by evolving the GBSSN variables according to a discrete approximation of the PDE system in Eq. (44). We can verify the accuracy of these simulations by monitoring the value of the constraint system in Eq. (45) at later times.

III. THE DISCONTINUOUS GALERKIN SCHEME

The chapter constructs a dG scheme for discretizing the GBSSN system and numerically solving the evolution equations. The first two sections consider a model PDE and describe general considerations for discretizing a PDE and dG methods in the context of this model system. The construction of a dG scheme for the GBSSN system is presented as a generalization of this construction at the end of Section B. Section C then describes the details of implementing this approach for solving the GBSSN system and presents both analytic details on the characteristics and hyperbolicity of the system and numerical details on the boundary conditions, filtering, and functions called numerical fluxes essential for the construction of a stable dG scheme.

A. Overview and Notation

The problem of simulating systems in general relativity has been reduced to evolving some initial data according to the GBSSN system. Our next task is to specify a scheme for performing this time evolution numerically on a computational grid with only a finite number of spatial points. In specifying such a scheme, we are in effect making two choices: 1-how to represent a solution $u(t, x)$ to the system by an approximate solution $u_h(t, x)$,

and 2-in what sense this approximate solution $u_h(t,x)$ will be made to satisfy the evolution system. To discuss this concretely but without the complexity of the GBSSN system we will consider a simple model system

$$\frac{\partial u}{\partial t} + \frac{\partial f(u)}{\partial x} = g(x) \tag{46}$$

throughout this section and the next. In this equation $u(t,x)$ is the solution to be determined, $f(u)$ represents a spatial flux and $g(x)$ acts as a (time-independent) source for the field u. An initial value problem is determined by specifying a spatial domain Ω on which we wish to solve the system, initial data $u_0 \equiv u(t=0,x)$ defined for all $x \in \Omega$, and some type of boundary conditions for u on the boundary $\partial\Omega$. Assume that Ω can be well-approximated by a discrete computational domain Ω_h. By specifying how to spatially discretize the system as an equation for u_h on $x \in \Omega_h$ we will obtain a semi-discrete scheme for solving Eq. (46). We will then be left with an ordinary differential equation for the time evolution of the system at each of the finitely many spatial points in Ω_h that can be discretized and solved by well-known and understood methods.

The oldest and simplest approach for spatial discretization is the finite difference scheme. In a finite difference scheme Ω_h is defined as a set of equally spaced grid points, $\Omega_h \equiv \{x^1, x^2 ..., x^K\}$. Denote the grid spacing by $h \equiv x^{k+1} - x^k$. We construct the numerical solution $u_h(t,x)$ by building local polynomials interpolating $u(t,x)$ at the grid points. For $x \in \left[x^{k-1}, x^{k+1}\right]$, define u_h by

$$u_h(t,x) \equiv \sum_{i=0}^{2} a_i(t)(x - x^k)^i. \tag{47}$$

Discretized fluxes f_h and source terms g_h are defined analogously. To describe the manner in which u_h is chosen to satisfy the PDE, define the residual $\mathcal{R}_h$ by

$$\mathcal{R}_h \equiv \frac{\partial u_h}{\partial t} + \frac{\partial f_h}{\partial x} - g_h(x). \tag{48}$$

The residual in effect measures the difference between the approximate and exact solution and will in general be nonzero since $u_h(t,x) \neq u(t,x)$. The natural statement to enforce for this scheme is that the residual vanish at each grid point $x^1, ..., x^K$. To define a (second order) finite difference scheme, we approximate the action of the spatial derivative operator at a grid point by the difference quotient of the function at two the surrounding grid points. The time evolution of u_h is then determined by enforcing that the residual vanish at each grid point to give

$$\frac{\partial u_h(x^k,t)}{\partial t} + \frac{f_h(x^{k+1},t) - f_h(x^{k-1},t)}{2h} - g_h(x^k) = 0. \tag{49}$$

While appealingly simple, there are drawbacks to the finite difference scheme, most notably a lack of geometric flexibility when constructing multidimensional grids and poor scaling of accuracy with resolution, as compared to dG and other methods in [32]. Taylor expanding $f_h(x^{k+1}) = f_h(x^k + h) = f_h(x) + hf'(x) + \frac{h^2}{2}f''(x) + \mathcal{O}(h^3)$ and $f_h(x^{k-1}) = f_h(x^k - h) = f_h(x^k) + hf'(x^k) + \frac{h^2}{2}f'' + \mathcal{O}(h^3)$ and substituting these expressions into the above equation shows that the error in making our finite difference approximation is $\mathcal{O}(h^2)$;

that is the approximate solution converges to the exact solution quadratically when we increase the spatial resolution by increasing the number of grid points. It is possible to improve this scaling by approximating u_h as a polynomial of higher order N, but this will require information from N grid points to solve for the N coefficients at each timestep. This will further restrict the geometry of the computational domain, and the error will still be on the order of some finite power of h. The scheme will therefore converge to the exact solution according to a power law.

One approach for improving the flexibility of the scheme is to divide the domain Ω into several smaller subdomains on which u_h is approximated by a higher order local polynomial that is disconnected from the polynomials in the adjacent subdomains. The discontinuous Galerkin (dG) scheme provides a method for this in which the residual on each subdomain is made to satisfy an integral condition known as a Galerkin condition that allows the approximate solution to converge toward the exact solution exponentially, a property known as spectral convergence. For a sufficiently smooth solution we can recover a meaningful global solution by integrating by parts to introduce boundary terms that can be used to couple adjacent subdomains. To describe this scheme precisely some notation additional is needed.

We follow the construction detailed in [32] and summarized in [23]. Given a one-dimensional physical domain $\Omega = [a, b] \subset \mathbb{R}$, we define a collection of K non-overlapping elements $\mathsf{D}^k = [a^k, b^k]$ with $a^1 = a$, $b^K = b$, and $b^{k-1} = a^k$ for $k = 2, ..., K$ that cover the domain. This splitting defines the computational domain Ω_h by

$$\Omega \simeq \Omega_h = \bigcup_{k=1}^{K} \mathsf{D}^k. \tag{50}$$

Define the local inner product and L^2 norm by

$$(u, v)_{\mathsf{D}^k} = \int_{\mathsf{D}^k} uv \, dx, \qquad ||u||^2_{\mathsf{D}^k} = (u, u)_{\mathsf{D}^k}. \tag{51}$$

Further define a global (broken) inner product and norm by

$$(u, v)_{\Omega_h} = \sum_{k=1} K \int_{\mathsf{D}^k} uv \, dx, \qquad ||u||^2_{\Omega^h} = (u, u)_{\Omega_h}. \tag{52}$$

These definitions hold for both scalar functions and vector valued functions so long as uv is then interpreted as $u \cdot v = u^T v$ for vectors.

Functions specified on the boundary between D^k and D^{k-1} or D^{k+1} will prove essential for constructing our scheme. In reference to a specific subdomain D^k, let u^- denote the interior solution on the boundary of D^k and let u^+ denote the exterior solution on the corresponding boundary of either D^{k-1} or D^{k+1}. Define the average across the boundary by

$$\{\{u\}\} = \frac{u^- + u^+}{2}, \tag{53}$$

and define a term describing the "jump" across the boundary by

$$[[u]] = \hat{\boldsymbol{n}}^- u^- + \hat{\boldsymbol{n}}^+ u^+, \tag{54}$$

where $\hat{\boldsymbol{n}}^-$ and $\hat{\boldsymbol{n}}^+$ are inward and outward pointing unit normal vectors respectively. Again the product should be interpreted as a scalar product for vector-valued solutions.

B. Constructing a Nodal dG Scheme

On each subdomain D^k we construct our approximate solution u_h^k as a local interpolating polynomial of specified order N

$$x \in \mathsf{D}^k : u_h^k(t,x) \equiv \sum_{i=0}^{N} u_h^k(t,x_i^k)\ell_i^k(x), \tag{55}$$

where ℓ_j^k is the jth Lagrange interpolating polynomial, defined in D^k by

$$\ell_j^k(x) \equiv \prod_{\substack{i=0 \\ i\neq j}}^{N} \frac{x - x_i^k}{x_j^k - x_i^k}. \tag{56}$$

This polynomial interpolates the exact solution u at the nodes x_j^k. Within each subdomain D^k these are distributed as Legendre-Gauss-Lobotto nodes, defined as the roots of the polynomial equation

$$(1-s^2)P_N'(s) = 0, \tag{57}$$

where P_N is the Nth Legendre polynomial. To map these nodes to the computational grid, we define an affine mapping from the interval $[-1,1]$ to D^k by

$$x^k(s) = a^k + \frac{1}{2}(1+s)(b^k - a^k). \tag{58}$$

This allows us to define our nodal points as $x_j^k = x^k(s_j)$. The global solution u_h is formally defined as

$$u_h(t,x) \equiv \bigoplus_{k=1}^{K} u_h^k(t,x). \tag{59}$$

For each subdomain D^k, define a residual $\mathcal{R}_h^k$ analogous to Eq. (48) by

$$\mathcal{R}_h^k \equiv \frac{\partial u_h^k(t,x)}{\partial t} + \frac{\partial f_h^k(u)}{\partial x} - g_h^k(x). \tag{60}$$

This specifies a discrete approximate of the solution and brings us to the second choice of how this approximate solution will be made to satisfy the PDE. The condition we will enforce is that the residual on each subdomain is orthogonal to a space of test functions on the subdomain. Choosing these test functions to be the Lagrange interpolating polynomials taken previously as our basis for u_h^k specifies what is called the kth Galerkin condition:

$$\left(\mathcal{R}_h^k, \ell_j^k\right)_{\mathrm{D}^k} = \int_{a^k}^{b^k} \left(\frac{\partial u_h^k(t,x)}{\partial t} + \frac{\partial f_h^k(u)}{\partial x} - g_h^k(x) \right) \ell_j(x)\, dx = 0 \quad \forall j. \tag{61}$$

Apart from the analytically known interpolating polynomials $\ell_i^k(x)$, the spatial dependence of the polynomial approximations u_h^k, f_h^k, and g_h^k is completely described by the values at the $N+1$ nodal points in each subdomain, and so these Galerkin conditions provide a set of $K(N+1)$ integral equations for the solution at each nodal point. This will become our semi-discrete scheme, though there is as of yet no coupling between the solutions in each

subdomain. To provide this coupling we look to incorporate information from the boundary of the subdomain into these integral conditions, and so we integrate the flux term by parts to give

$$\int_{a^k}^{b^k} \left[\frac{\partial u_h^k(t,x)}{\partial t} \ell_j^k(x) - f_h^k(u) \frac{\partial \ell_j^k(x)}{\partial x} - g_h^k(x) \ell_j^k(x) \right] dx + \left[f_h^k(u) \ell_j^k(x) \right|_{a^k}^{b^k} = 0. \tag{62}$$

Rather than enforce this precise condition, we define a numerical flux $f_h^*(u)$ that will incorporate information from the subdomains adjacent to D^k and enforce

$$\int_{a^k}^{b^k} \left[\frac{\partial u_h^k(t,x)}{\partial t} \ell_j^k(x) - f_h^k(u) \frac{\partial \ell_j^k(x)}{\partial x} - g_h^k(x) \ell_j^k(x) \right] dx + \left[f_h^*(u) \ell_j^k(x) \right|_{a^k}^{b^k} = 0. \tag{63}$$

The numerical flux f_h^* is only featured in the boundary term of this expression and is therefore only defined on the boundaries of D^k. To provide the desired coupling between subdomains it is defined to be a function of the interior and exterior solutions at each boundary, that is $f_h^* = f_h^*(u^+, u^-)$. The stability of a dG scheme depends upon the choice of f_h^*, and we will delay discussing the numerical fluxes chosen for solving the GBSSN system until the next section. Employing a second integration by parts provides the integral equations

$$\int_{a^k}^{b^k} \left(\frac{\partial u_h^k(t,x)}{\partial t} + \frac{\partial f_h(u)}{\partial x} - g_h^k(x) \right) \ell_j^k(x) dx + \left[\left(f_h^*(u) - f_h(u) \right) \ell_j^k(x) \right|_{a^k}^{b^k} = 0. \tag{64}$$

This defines the form of the Galerkin conditions that we enforce.

Note that solution u is approximated in D^k as an N-degree polynomial u_h^k and the source $g(x)$ can naturally be approximated as an N-degree polynomial g_h^k by defining a straightforward analog of Eq. (55). If the flux $f(u)$ contains any products of the form $a(x)b(x)$, as the nonlinear GBSSN system certainly does, it would naturally be expressed as a polynomial of degree $2N$ or higher. In order to keep $f_h(x)$ in the span of our basis of degree N Lagrange polynomials, we must replace any products of interpolated polynomials with interpolations of the product function like

$$(a(t,x)b(t,x))_h^k = a_h^k(t,x) b_h^k(t,x) \to \sum_{i=0}^{N} a_h(t, x_i^k) b_h(t, x_i^k) \ell_i^k(x). \tag{65}$$

These two expressions are not equivalent and this interpolation of products results in what is known as aliasing error. Aliasing error in dG is discussed in [32], and the next section introduces an exponential filter to prevent any resulting aliasing-driven numerical instabilities. Using the above prescription any flux or source terms in an arbitrary non-linear PDE can still be approximated by N-degree polynomials interpolated at the nodal points. Furthermore, since the nodal values of product functions are found by multiplying the nodal values of each factor pointwise, we need only consider the $K(N+1)$ nodal values for each evolved variable.

We can therefore represent our solution u_h^k as a vector of its values at the nodal points by taking

$$u_h^k(t,x) = \boldsymbol{u}^k(t)^T \boldsymbol{\ell}^k(x), \tag{66}$$

where the vectors $\boldsymbol{u}^k(t)$ and $\boldsymbol{\ell}^k(x)$ are given by

$$\boldsymbol{u}^k(t) = \left[u^k(t, x_0^k), ..., u^k(t, x_N^k) \right]^T, \qquad \boldsymbol{\ell}^k(x) = \left[\ell_0^k(x), ..., \ell_N^k(x) \right]^T, \tag{67}$$

noting that at the nodal points $u^k(t, x_i^k) = u_h^k(t, x_i^k)$. In this representation, Eq. (64) becomes a set of $N+1$ ODEs for the coefficients $\boldsymbol{u}^k(t)$ in each subdomain. Furthermore, since there is no spatial dependence in these coefficients themselves we can therefore carry out the spatial integration in Eq. (64) independently from the time integration. To this end, define the mass and stiffness matrices $\mathcal{M}^k$ and $\mathcal{S}^k$ on the k-th subdomain by

$$\mathcal{M}_{ij}^k = \int_{a^k}^{b^k} dx\ \ell_i^k(x)\ell_j^k(x), \qquad \mathcal{S}_{ij}^k = \int_{a^k}^{b^k} dx\ \ell_i^k(x)\frac{\partial \ell_j^k}{\partial x}. \tag{68}$$

Since spatial derivatives will only affect the nodal basis functions $\ell^k(x)$, we can also build a matrix $\mathcal{D}^k$ that acts as a numerical spatial derivative operator. In terms of the above matrices this derivative matrix is given by

$$\mathcal{D}_{ij}^k = \left.\frac{\partial \ell_j^k}{\partial x}\right|_{x=x_i^k} = \sum_{m=1}^{N+1} \left(\mathcal{M}^k\right)_{im}^{-1} \mathcal{S}_{mj}. \tag{69}$$

We can now express the semi-discrete evolution equations in each subdomain as the matrix equation

$$\partial_t \boldsymbol{u}^k = \mathcal{D}^k \boldsymbol{f}^k(\boldsymbol{u}^k) + \boldsymbol{g}^k + \left(\mathcal{M}^k\right)^{-1} \boldsymbol{\ell}^k \left[\boldsymbol{f}^k(\boldsymbol{u}^k) - \boldsymbol{f}^*(u^+, u^-)\right]_{a^k}^{b^k}. \tag{70}$$

Though throughout this section we have worked with the toy system given by Eq. (46), the construction of a nodal dG scheme for solving the GBSSN system is a straightforward generalization. Each evolved variable is approximated by a local interpolating polynomial defined on each subdomain, and the evolution equation for each evolved variable in Eq. (44) can be used to define a residual for that variable on each subdomain. By enforcing the Galerkin condition that the inner product of each residual with the N Lagrange interpolating polynomials that act as our basis functions and introducing a numerical flux for each field we can form a discretized evolution equation. These will be close analogs to Eq. (70), though now the flux and source vector analog of $\boldsymbol{f}(\boldsymbol{u})$ in each equation will be a functions of all the evolved fields.

There is one significant complication in constructing a dG scheme for solving the GBSSN system not present in our model system: the flux is assumed to be an algebraic function of the evolved system variables, but the GBSSN system includes second order spatial derivatives. This discrepancy is resolved by defining auxiliary variables representing the spatial derivatives of each field for which second derivatives appear. We define an auxiliary lapse function for example as $Q_\alpha \equiv \partial_r \alpha$. These auxiliary variables are not themselves evolved in the second order scheme presented in [23] and used in many of the simulations to follow. They are instead computed from the evolved variables at each step of the time evolution by defining a residual on the k-th subdomain for each auxiliary variable straight from its definition. For Q_α this residual is defined as

$$\left(\mathcal{R}_{Q_\alpha}\right)_h^k = -\left(Q_\alpha\right)_h^k + \partial_r \alpha_h^k. \tag{71}$$

As with the residuals defined by the evolution equations, we enforce a Galerkin condition $\left((\mathcal{R}_{Q\alpha})_h^k, \ell_j\right)_{\mathrm{D}}^k = 0$ for all j and introduce a numerical flux $\alpha_h^*(\alpha^+, \alpha^-)$ to solve for the nodal values like

$$\boldsymbol{Q}_\alpha = \mathcal{D}^k \boldsymbol{\alpha} + \left(\mathcal{M}^k\right)^{-1} \boldsymbol{\ell}^k \left[\boldsymbol{\alpha}^* - \boldsymbol{\alpha}\right]_{a^k}^{b^k}, \tag{72}$$

where we have suppressed the subdomain index k and any functional dependencies. In the first order scheme presented in Chapter VI, the auxiliary fields like Q_α are promoted to independently evolved system variables with their own discretized evolution equations in place of the above equation.

The discrete evolution equations for the evolved fields in the GBSSN system can now be constructed as analogs of Eq. (70) using the techniques of this section. As a representative example, the evolution equation for K is discretized as

$$\begin{aligned}\partial_t \boldsymbol{K} = \boldsymbol{\beta}^r \mathcal{D}^k \boldsymbol{K} - \frac{\boldsymbol{\chi} \mathcal{D}^k \boldsymbol{Q}_\alpha}{\boldsymbol{g}_{rr}} + \frac{\boldsymbol{\chi} \boldsymbol{Q}_{g_{rr}} \boldsymbol{Q}_\alpha}{2\boldsymbol{g}_{rr}} - \frac{\boldsymbol{\chi} \boldsymbol{Q}_{g_{\theta\theta}} \boldsymbol{Q}_\alpha}{\boldsymbol{g}_{rr} \boldsymbol{g}_{\theta\theta}} \\ + \frac{\boldsymbol{Q}_\alpha \boldsymbol{Q}_\chi}{2\boldsymbol{g}_{rr}} + \frac{3\boldsymbol{\alpha} \boldsymbol{A}_{rr}^2}{2\boldsymbol{g}_{rr}^2} + \frac{1}{3}\boldsymbol{\alpha} \boldsymbol{K}^2 + (\mathcal{M}^k)^{-1} \boldsymbol{\ell}^k \left[\boldsymbol{f}_K - \boldsymbol{f}_K^* \right|_{a^k}^{b^k} . \end{aligned} \tag{73}$$

The index k is again suppressed, and products of vectors in this expression are to be interpreted as pointwise products as described in Eq. (65).

We are now just left with an ordinary differential equation for the time evolution of each evolved GBSSN variable at each grid point. Discretizing the time evolution is schematically accomplished by calculating the change in each variable over a small but finite timestep Δt by substituting the field values at time t into the above semi-discrete equation and its analogs for the other variables, adding this change to find the fields at $t + \Delta t$, and iterating this process to find the fields at a desired later time. The simulations presented in this thesis use a fourth-order Runge-Kutta method to perform the time evolution, a common choice for performing time integration in computational physics and described in the context of a dG scheme in [32]. Numerical stability depends upon the choice of timestep.

The last major general property of dG methods to be described is the convergence with polynomial order N. A proof of the spectral convergence of dG methods is given in [32]; we will simply sketch out the main points. From the properties of the Legendre polynomial P_j, it can be shown that any function u can be approximated by a weighted sum of the first N Legendre polynomials denoted u^*, the "best approximating polynomial of order N", on the subdomain D^k with an error bounded like

$$||u - u^*||_{\mathsf{D}^k} \leq C(t)(h_k)^{N+1}, \tag{74}$$

where h_k is the length of D^k and $C(t)$ is a (time-dependent) constant. An arbitrary nodal representation u_{nodal} of u using the first N Lagrange interpolating polynomials can then be shown to approximate U with an error bounded like

$$\max_{x \in \mathsf{D}^k} |u - u_{nodal}| \leq (1 + \Lambda) \max_{x \in \mathsf{D}^k} |u - u^*|, \tag{75}$$

where the constant Λ depends only on the nodal points chosen. The Legendre-Gauss-Lobotto nodal points are defined precisely as the nodal points that minimize Λ, and so our interpolation error does not differ significantly from the error of the best approximating polynomial u^*. This allows us to bound the error of our nodal representation u_h^k like

$$||u - u_h^k||_{\mathsf{D}^k} \leq \tilde{C}(t)(h_k)^{N+1}, \tag{76}$$

where $\tilde{C}(t)$ is a new time-dependent constant. This verifies that the error between the exact solution and our numerical approximation decreases exponentially with N and so a nodal dG scheme possess spectral convergence. The error also depends on the size of the subdomains

and increasing the number of subdomains will decrease the numerical error as well, though the convergence in this case may depend on the details of the subdomain construction and how the numerical error is distributed through the domain.

Finally, this idea of approximating a function using a basis of Legendre polynomials leads us to discuss an equivalent modal representation of the solution u that will be used in the next section when we discuss filtering. We can express $u_h^k(t,x)$ in a basis of Legendre polynomials $P_j(x)$ like

$$u_h^k(t,x) = \sum_{j=0}^{N} u(t,x_j^k)\ell_j^k(x) = \sum_{j=0}^{N} \hat{u}_j^k(t)P_j(x), \tag{77}$$

where the $\hat{u}_j^k$ are called the modal coefficients of the system and can be calculated from the above relation to the nodal representation. Modal coefficients for larger k correspond to the coefficients of higher-order Legendre polynomials and therefore to the higher-frequency modes of the solution.

C. Details of a dG Scheme for GBSSN

1. *Wavespeeds and Characteristics*

We first consider a few analytic properties of the GBSSN system relevant to our numerical simulations, namely the characteristic variables and wavespeeds of the system and strong hyperbolicity, a necessary condition for the well-posedness of an initial problem. These are properties of the GBSSN system itself rather than of any particular discretization of it. To carry out this analysis with a minimum of notational clutter, we define an abstract representation of the GBSSN system using the column vectors

$$u = \begin{pmatrix} \chi \\ g_{rr} \\ g_{\theta\theta} \\ \alpha \\ \beta^r \end{pmatrix}, \qquad v = \begin{pmatrix} B^r \\ A_{rr} \\ K \\ \Gamma^r \end{pmatrix}, \qquad Q = u' = \begin{pmatrix} \chi' \\ g'_{rr} \\ g'_{\theta\theta} \\ \alpha' \\ \beta^{r\prime} \end{pmatrix}, \qquad W = \begin{pmatrix} u \\ v \\ Q \end{pmatrix}. \tag{78}$$

Note that these are vectors of functions of the coordinates (t,r) rather than vectors of points in the computational domain as were considered previously. In particular W corresponds to the solution u of the model system in the last section rather than the vector $\boldsymbol{u}$ of its values at nodal points. While in our second order simulations the auxiliary sector Q is constructed at each timestep, many theoretical tools for analysis of PDEs are developed only for fully first order PDEs. In particular the notion of strong hyperbolicity of a second order system is defined in the context of the strong hyperbolicity of possible first order reductions of the system. In this section we will therefore consider a first order reduction of GBSSN in which Q is independently evolved, found by making the replacements $u' \to Q$, $u'' \to Q'$ in the GBSSN system. For a detailed discussion of characteristics, hyperbolicity, boundary conditions, and associated topics for second order systems in the context of numerical relativity see [27, 28].

In this notation we can write the GBSSN system as a matrix analog of the model system given by Eq. (46). Since each term in Eq. (44) is linear in terms involving spatial derivatives

v' and Q' and the coefficients of these terms depend only on u, we can define a matrix $A(u)$ and a source vector $S(W)$ to express the GBSSN system as

$$\partial_t W + A(u)W' = S(W). \tag{79}$$

In this notation the physical fluxes like f_K are given by the corresponding components of $A(u)W$. The homogeneous part of this equation, $\partial_t W + A(u)W' = 0$ is called the principle part of the equation.

If the matrix $A(u)$ were diagonal, then the principle part of the system would de-couple the fields so that each evolved variable would independently satisfy an equation analogous to the model system. So long as $A(u)$ is diagonalizable, we can transform the solution vector W into the eigenbasis of $A(u)$ in which the flux has this simple form. The components of W in the eigenbasis of $A(u)$ are called the characteristic variables of the system and denoted by X_i. The corresponding eigenvalues of $A(u)$ are called the characteristic speeds, or more suggestively wavespeeds, and will be denoted by μ_i with the set of eigenvalues denoted $\mu(A)$. Considering only the principle part of the system, the X_i satisfy $\partial_t X_i = -\mu_i \partial_r X_i$ and so they define integral curves in the phase space of the system that a solution will move along with velocity $-\mu_i$ as it evolves in time. When $\max|\mu(A)|$ is larger, the area of the computational domain causally connected to a given point in a fixed length of time will be larger. Since the spatial resolution of a numerical scheme is fixed independently of the wavespeeds of the system, this suggests that a smaller timestep may be necessary to maintain stability, and the choice of timestep in our numerical simulations is therefore guided by $\max|\mu(A)|$.

Since all instances of u' in the GBSSN system have been replaced with Q, the upper-left 5x5 block of $A(u)$ will be the zero matrix. This makes each field in u a characteristic variable of the system with wavespeed 0. The remaining 9 characteristic variables and corresponding wavespeeds are found by diagonalizing the non-degenerate 9x9 block of $A(u)$. The eigenvalues of this block are given by

$$\begin{gathered} \mu_1 = 0, \qquad \mu_2 = -\beta^r, \qquad \mu_3 = -\beta_r, \\ \mu_4^{\pm} = -\beta^r \pm \sqrt{\tfrac{2\alpha\chi}{g_{rr}}}, \qquad \mu_5^{\pm} = -\beta^r \pm \alpha\sqrt{\tfrac{\chi}{g_{rr}}}, \qquad \mu_6^{\pm} = -\beta^r \pm \sqrt{\tfrac{\lambda}{g_{rr}}}. \end{gathered} \tag{80}$$

The characteristic variables can be calculated by finding the matrix of eigenvalues used to diagonalize $A(u)$ and then applying this matrix to the state vector W to give[4]

$$X_1 = g_{\theta\theta} Q_{g_{rr}} + 2 g_{rr} Q_{g_{\theta\theta}}, \tag{81a}$$

$$X_2 = g_{rr}\Gamma^r + \frac{2}{\chi} Q_\chi - \frac{1}{2 g_{rr} Q_{g_{rr}}} - \frac{1}{g_{\theta\theta}} Q_{g_{\theta\theta}}, \tag{81b}$$

$$X_3 = \frac{g_{rr}}{\lambda} B^r + \frac{2}{\chi} Q_\chi - \frac{1}{2 g_{rr}} Q_{g_{rr}} + \chi - \frac{1}{g_{\theta\theta}} Q_{g_{\theta\theta}}, \tag{81c}$$

$$X_4^{\pm} = \pm\sqrt{\frac{2\alpha g_{rr}}{\chi}} K + Q_\alpha, \tag{81d}$$

[4] This calculation is carried out in some detail in Appendix A of [23]. For a detailed description of the process of finding the characteristic variables and wavespeeds for a simpler system and using them to construct Sommerfeld boundary conditions, see our derivation of the characteristic variables for the Klein-Gordon equation in section VII B 3

$$X_5^{\pm} = \mp \frac{3}{\sqrt{g_{rr}\chi}} A_{rr} \pm 2\sqrt{\frac{g_{rr}}{\chi}} K + 2 g_{rr}\Gamma^r + \frac{1}{\chi} Q_\chi - \frac{1}{g_{rr}} Q_{g_{rr}} + \frac{1}{g_{\theta\theta}} Q_{g_{\theta\theta}}, \tag{81e}$$

$$X_6^{\pm} = -\frac{3}{4}\frac{g_{rr}}{\lambda} B^r \pm \frac{\alpha\sqrt{\lambda g_{rr}}}{2\alpha\chi - \lambda} K - \frac{\beta^r}{8\left(\beta^r g_{rr} \mp \sqrt{\lambda g_{rr}}\right)} Q_{g_{rr}} \tag{81f}$$
$$- \frac{\beta^r g_{rr}}{4 g_{\theta\theta}\left(\beta^r g_{rr} \mp \sqrt{\lambda g_{rr}}\right)} Q_{g_{\theta\theta}} + \frac{\alpha\chi}{2\alpha\chi - \lambda} Q_\alpha \pm \sqrt{\frac{g_{rr}}{\lambda}} Q_{\beta^r}.$$

It will further prove useful to express the evolved fields in v and Q in terms of u and the characteristic variables. Inverting the above system gives

$$B^r = -\frac{1}{6}\frac{\lambda}{g_{rr} g_{\theta\theta}}\left[\frac{(\beta^r)^2}{(\beta^r)^2 g_{rr} - \lambda}\right] X_1 + \frac{2\lambda\alpha\chi}{3 g_{rr}(2\alpha\chi - \lambda)}\left(X_4^+ + X_4^-\right) - \frac{2\lambda}{3 g_{rr}}\left(X_6^+ + X_6^-\right) \tag{82a}$$

$$A_{rr} = \frac{1}{3}\sqrt{\frac{g_{rr}\chi}{2\alpha}}\left(X_4^+ - X_4^-\right) - \frac{\sqrt{g_{rr}}\chi}{6}\left(X_5^+ - X_5^-\right) \tag{82b}$$

$$K = \sqrt{\frac{\chi}{8\alpha g_{rr}}}\left(X_4^+ - X_4^-\right) \tag{82c}$$

$$\Gamma^r = -\frac{1}{6 g_{rr} g_{\theta\theta}}\left[\frac{(\beta^r)^2}{(\beta^r)^2 g_{rr} - \lambda}\right] X_1 + \frac{1}{g_{rr}}\left(X_2 - X_3\right) + \frac{2\alpha\chi}{3 g_{rr}(2\alpha\chi - \lambda)}\left(X_4^+ + X_4^-\right) \tag{82d}$$
$$- \frac{2}{3 g_{rr}}\left(X_6^+ + X_6^-\right)$$

$$Q_\chi = \frac{\chi}{12 g_{rr} g_{\theta\theta}}\left[\frac{4(\beta^r)^2 g_{rr} - 3\lambda}{(\beta^r)^2 g_{rr} - \lambda}\right] X_1 + \frac{\chi}{2} X_3 - \frac{\alpha\chi^2}{3(2\alpha\chi - \lambda)}\left(X_4^+ + X_4^-\right) \tag{82e}$$
$$+ \frac{\chi}{3}\left(X_6^+ + X_6^-\right)$$

$$Q_{g_{rr}} = \frac{2(\beta^r)^2 g_{rr} - 3\lambda}{6 g_{\theta\theta}((\beta^r)^2 g_{rr} - \lambda)} X_1 + \frac{4}{3} g_{rr} X_2 - g_{rr} X_3 + \frac{2\alpha\chi g_{rr}}{3(2\alpha\chi - \lambda)}\left(X_4^+ + X_4^-\right) \tag{82f}$$
$$- \frac{1}{3} g_{rr}\left(X_5^+ + X_5^-\right) - \frac{2}{3} g_{rr}\left(X_6^+ + X_6^-\right)$$

$$Q_{g_{\theta\theta}} = \left[\frac{1}{4 g_{rr}} + \frac{(\beta^r)^2}{12((\beta^r)^2 g_{rr} - \lambda)}\right] X_1 - \frac{2}{3} g_{\theta\theta} X_2 + \frac{1}{2} g_{\theta\theta} X_3 - \frac{\alpha\chi g_{\theta\theta}}{3(2\alpha\chi - \lambda)}\left(X_4^+ + X_4^-\right) \tag{82g}$$
$$+ \frac{1}{6} g_{\theta\theta}\left(X_5^+ + X_5^-\right) + \frac{1}{3} g_{\theta\theta}\left(X_6^+ + X_6^-\right)$$

$$Q_\alpha = \frac{1}{2}\left(X_4^+ + X_4^-\right) \tag{82h}$$

$$Q_{\beta^r} = \frac{\beta^r \lambda}{8 g_{rr} g_{\theta\theta}((\beta^r)^2 g_{rr} - \lambda)} X_1 - \frac{\lambda}{(2\alpha\chi - \lambda)}\sqrt{\frac{\alpha\chi}{8 g_{rr}}}\left(X_4^+ - X_4^-\right) + \frac{1}{2}\sqrt{\frac{\lambda}{g_{rr}}}\left(X_6^+ - X_6^-\right). \tag{82i}$$

For our purposes the system can be considered strongly hyperbolic so long as the matrix $A(u)$ is diagonalizable with real eigenvalues and a complete basis of eigenvectors. An in-depth discussion of the hyperbolicity of the GBSSN system in given in [22]. Maintaining real eigenvalues and non-singular eigenvectors requires that χ, g_{rr}, and $g_{\theta\theta}$ be non-zero and

additional imposes the following conditions on λ:

$$\lambda > 0, \qquad (\beta^r)^2 g_{rr} - \lambda \neq 0, \qquad 2\alpha\chi - \lambda \neq 0. \tag{83}$$

These second two conditions are not explicitly enforced in the scheme and may actually be violated, but the points of violation in effect form a set of measure zero within the computational domain and no instabilities have been observed to result from this violation.

We see also that the system admits an inner excision surface, a surface at which all wavespeeds are nonpositive, provided

$$\beta^r \geq \max\left(\sqrt{\frac{2\alpha\chi}{g_{rr}}}, \alpha\sqrt{\frac{\chi}{g_{rr}}}, \sqrt{\frac{\lambda}{g_{rr}}}\right). \tag{84}$$

Choosing λ sufficiently small guarantees the existence of such a surface, and the value of λ further determines the location of the excision surface. Note in particular that $\mu_5^+ = -\beta^r + \alpha\sqrt{\frac{\chi}{g_{rr}}}$ is the velocity of a radially outward null geodesic as given by Eq. (42), and so at an excision surface all causal information must have a non-positive coordinate velocity. More will be said on this in Chapter IV.

2. Numerical Flux

In this section we define the numerical fluxes for both the first and second order schemes. In both cases we take $f_u^* = f_u = 0$ and take f_v^* to be

$$f_v^* = \{\{f_{v,h}\}\} + \frac{\tau}{2}[[v_h]], \tag{85}$$

and in the first order reduction we similarly take

$$1^{\text{st}}\text{order}: \qquad f_Q^* = \{\{f_{Q,h}\}\} + \frac{\tau}{2}[[Q_h]]. \tag{86}$$

This is a common form for numerical fluxes in dG that averages the field v across the boundary and then adds a term "penalizing" jumps across subdomains. A proper choice of the penalty term $\tau(x)$ provides a negative contribution to the L_2 norm of the energy of the system to damp growth in the solution and ensure numerical stability. Choosing a numerical flux for a dG scheme is discussed in detail in [32]. For further discussion of the stability of GBSSN with this flux choice see [23], especially Appendix B in which a proof of stability is given for a model scheme that employs this flux. More general analysis of this numerical flux is also given in [3].

A local Lax-Friedrichs flux is defined by choosing $\tau(x) \geq \max|\mu(\nabla_W F(W(x))|$, and is a common choice for fully first order systems [31]. Our flux is given by $F(W) = A(u)W$, which is linear for v and Q and vanishes for u, and so this consideration becomes $\tau(x) \geq \max|\mu(A(u))|$. At the boundary between D^k and D^{k+1}, we therefore choose

$$\tau(b^k) = \tau(a^{k+1}) = C \cdot \max|\mu(A(u))|, \tag{87}$$

where C is an $\mathcal{O}(1)$ constant chosen for numerical stability. Note that the max in this expression should be taken over both $A(u^+)$ and $A(u^-)$. Since the auxiliary variables are

not evolved independently in the second order scheme, there is no need to incorporate the additional damping provided by τ in the auxiliary fluxes, and so for these terms we employ a simple penalized central flux

$$2^{\text{nd}}\text{order}: \qquad f_Q^* = \{\{u_h\}\} - \frac{1}{2}[[u_h]]. \tag{88}$$

3. Boundary Conditions

Finding suitable boundary conditions for the (G)BSSN system is highly non-trivial. In particular finding outer boundary conditions that fix incoming radiation to zero, control constraint growth, and specify desired gauge choices is an active area of research; for a review see [41]. Our choices will be strongly guided by considerations of numerical stability, and the particular choice of boundary conditions made for each simulation will be discussed in later chapters.

The boundary subdomains D^1 and D^K are coupled to the exterior of the computational domain through the numerical flux at those boundaries. Imposing boundary conditions on a dG scheme is therefore accomplished by specifying the external solution W^+ that is used to calculate the numerical flux at the outer boundary of these subdomains. If a boundary is contained within an excision surface, then no information from W^+ should propagate into the domain. There will certainly be no flow of causal information into the computational domain from the boundary, and so on physical grounds we can safely take $W^+ = W^-$.

Apart from this (very important) case, we consider two choices for W^+. If an analytic solution W_{exact} is known, we can impose exact boundary conditions by taking $W^+ = W_{\text{exact}}$. If the system does not have a known analytic solution, an intuitive condition to enforce is that no new information should enter the computational domain from the exterior solution, known as a "no incoming radiation" condition. This cannot be simply enforced in the presence of non-zero source terms, and so we consider Sommerfeld boundary conditions that are designed to enforce that there is no incoming radiation in the principle part of the system. Assuming that we are at the outer boundary of our domain, Sommerfeld boundary conditions are defined by specifying that the incoming characteristics of the external solution are 0: $X_2 = X_3 = X_4^- = X_5^- = X_6^- = 0$ and the zero speed and outgoing characteristics of the external solution match those of the numerical solution at the boundary $X_1 = X_1(W^-)$, $X_4^+ = X_4^+(W^-)$, $X_5^+ = X_5^+(W^-)$, $X_6 = X_6^+(W^-)$. The outgoing characteristic variables of the numerical solution are calculated using Eq. (81), and we can then construct W^+ according to these specifications on the characteristics by using Eq. (82).

4. Filtering

By approximating products of degree N polynomials as degree N polynomials as in Eq. (65), aliasing error is introduced to the scheme. Since it is higher degree terms that are effectively ignored, this aliasing error will be concentrated in the higher degree modes of our approximate solution when using the modal representation defined in Eq. (77) by taking the Legendre polynomials as basis functions instead of Lagrange interpolating polynomials. A straightforward way to control aliasing-driven instabilities is therefore to damp the high degree modal coefficients. To this end let $\eta_j = j/N$ and define an exponential filter function

σ by

$$\sigma(\eta_j) = \begin{cases} 1 & \text{for } 0 \leq \eta_j \leq N_c/N \\ \exp\left(-\epsilon\left(\frac{\eta_j - N_c/N}{1-N_c/N}\right)^{2s}\right) & \text{for } N_c/N \leq \eta_j \leq 1 \end{cases}, \tag{89}$$

where $\epsilon \simeq -\log(\varepsilon_{\text{mach}}) = 36$ and $\varepsilon_{\text{mach}}$ is machine accuracy in double precision. This filter exponentially damps the highest $N - N_c$ modes with the damping strength dependent on the parameter s. We take N_c and s as problem-dependent numerical parameters chosen for stability. In our numerical simulations we apply this filter by transforming to the modal representation, scaling the modal coefficients $\hat{u}_j^k$ by $\sigma(\eta_j)$ in each subdomain, and transforming back. This transformation and filtering in dG schemes is described in more detail in [32]. For our purposes it is enough to note that with proper choices of N_c and s this filter is sufficient to control aliasing-driven instabilities in the numerical simulations considered below.

IV. BLACK HOLES AND TURDUCKENING

We are now equipped with a numerical scheme suitable for approximately solving the GBSSN system. This chapter describes the final considerations necessary for defining initial value problems involving black holes and constructing our numerical simulations: building initial data describing a black hole and managing the singularities present in this initial data through the excision and turduckening techniques.

A. Overview

A central motivation for this work is the development of techniques that can be used to construct a computationally efficient scheme for modeling binary black hole systems. The computational difficulties in binary black hole simulations primarily stem from the presence of singularities in the computational domain resulting from divergences in the physical metric at the center of a black hole. Since there is no way to do meaningful numerical computations with infinities, simulations of black holes require some way of either smoothing out this singularity or removing it from the computational domain. Most techniques for managing singularities with either approach rely on the fact that the geometry of spacetime near a black hole will include an event horizon, a surface inside which all causal paths move inwards towards the central singularity. The exterior of the event horizon is causally disconnected from the interior. Since the physically interesting information to extract from black hole simulations is generally the gravitational radiation or other signals as they would appear to an observer far away from the black hole, the interior solution may be freely modified with no loss of relevant information as long as these modifications do not affect the exterior solution.

Our work follows that of Field et. al. in [23], in which a nodal dG scheme is used to carry out simulations of a black hole in spherical symmetry. This provides a useful model system for constructing dG black hole simulations since there is a known analytic solution that can be directly compared to the numerical solution. These simulations manage the black hole singularity through a technique called excision in which a region surrounding the singularity is removed from the computational domain entirely. This is simple to implement for a black hole in spherical symmetry, but in binary black hole simulations the singularities will move

throughout the computational domain and finding a suitable region to be excised at each timestep requires a computationally intensive process of horizon tracking. For this reason state-of-the-art BSSN simulations do not use excision.

We will consider an alternative method of managing singularities called "turduckening" that has been developed in [14, 15]. The singular initial data for the interior of a black hole's event horizon is not evolved, and the black hole is instead "stuffed" with smooth but constraint violating initial data. Simulating a black hole in spherically symmetry is a useful model problem for studying how turduckening affects the stability and convergence of our dG scheme, so to allow for easy comparisons to the excision simulations of [23] we will follow the construction of black hole initial data in Kerr-Schild coordinates for a spherically symmetric spacetime detailed in Appendix B of [23].

B. Constructing Initial Data

Consider an uncharged, nonspinning black hole, known as a schwarzschild black hole. We adopt Kerr-Schild coordinates, directly related to incoming Eddington-Finkelstein null coordinates, in which the line element for a mass M Schwarzschild black hole centered at $r = 0$ is given by

$$ds^2 = -\alpha^2 dt^2 + \left(1 + \frac{2M}{R}\right)\left(dR + \beta^R dt\right)^2 + R^2 d\theta^2 + R^2 \sin^2\theta d\phi^2, \tag{90}$$

where R is the areal radius, $\alpha = (1 + 2M/R)^{-1/2}$ is the lapse, and $\beta^R = 2M/(R + 2M)$ is the shift vector in these coordinates. The physical spatial metric $\bar{g}_{ij}$ is given by the spatial part of the line element. schwarzschild black holes are time-independent solutions of the Einstein field equations, so the GBSSN variables describing this spacetime will provide a time-independent solution to the GBSSN system.

To construct the GBSSN variables for this spacetime, we first apply the conformal decomposition $g_{ij} = \chi \bar{g}_{ij}$ to relate the spatial part of the line element in conformal coordinates (r, θ, ϕ) and areal coordinates (R, θ, ϕ) as

$$dr^2 + r^2(d\theta^2 + \sin^2\theta d\phi^2) = \chi\left[\left(1 + \frac{2M}{R}\right) dR^2 + R^2 d\theta^2 + R^2 \sin^2\theta d\phi^2\right]. \tag{91}$$

The angular piece of this equation defines the conformal radius r by $\chi R^2 = r^2$, while the radial piece provides an ordinary differential equation for $\frac{dR}{dr}$. We can apply the first relation to eliminate χ from the radial equation to give

$$\left(\sqrt{1 + \frac{2M}{R}}\right)\frac{dR}{R} = \frac{dr}{r}. \tag{92}$$

We can integrate this equation to solve for $r(R)$ as

$$r = \frac{R}{4}\left(1 + \sqrt{1 + \frac{2M}{R}}\right)^2 e^{2 - 2\sqrt{1 + 2M/R}}. \tag{93}$$

With this we can then determine $\chi(R) = \frac{r(R)^2}{R^2}$. We can then calculate Γ^r from Eq. (40) and K and A_{rr} from Eq. (15) and the conformal decomposition in Eq. (38). Choosing $B^r = 0$ then completely specifies the initial data for evolved GBSSN variables as

$$\alpha = \left(1 + \frac{2M}{R}\right)^{-\frac{1}{2}} \tag{94a}$$

$$\beta^r = \beta^R \frac{dr}{dR} = \sqrt{\chi}\left(1 + \frac{2M}{R}\right)^{-\frac{1}{2}} \frac{2M}{R} \tag{94b}$$

$$g_{rr} = 1 \tag{94c}$$

$$g_{\theta\theta} = r^2 = \chi R^2 \tag{94d}$$

$$\chi = \frac{1}{16}\left(1 + \sqrt{1 + \frac{2M}{R}}\right)^4 e^{4-4\sqrt{1+2M/R}} \tag{94e}$$

$$B^r = 0 \tag{94f}$$

$$A_{rr} = -\left(1 + \frac{2M}{R}\right)^{-\frac{1}{2}} \frac{4M}{3R^2}\left(\frac{2R+3M}{R+2M}\right) \tag{94g}$$

$$K = \left(1 + \frac{2M}{R}\right)^{-\frac{3}{2}} \left(1 + \frac{3M}{R}\right) \frac{2M}{R^2} \tag{94h}$$

$$\Gamma^r = -\frac{2}{r} = -\frac{2}{R\sqrt{\chi}}. \tag{94i}$$

Calculating the exact values of the auxiliary fields, used to impose exact boundary conditions in the second order scheme and to construct initial data for the first order simulations presented in Chapter VI, requires us to take derivatives of the above expressions with respect to the conformal radius r. Re-arranging Eq. (92) gives

$$\frac{dR}{dr} = \chi^{-\frac{1}{2}}\left(1 + \frac{2M}{R}\right)^{-\frac{1}{2}}. \tag{95}$$

The necessary r-derivatives can then be calculated by taking derivatives with respect to R and applying the chain rule. To actually construct this initial data for a specified r-coordinate domain, we must first invert Eq. (93) in order to find $R(r)$. This cannot be done analytically, and so we use Newton's method to numerically invert the equation.

Inspecting the above system for the initial data, the fields K, A_{rr}, and Γ^r are clearly divergent as $r \to 0$. χ contains a superficially divergent factor but actually approaches 0 as $r \to 0$, as is expected since the physical metric, inversely related to χ, diverges. β^r also approaches 0 despite containing superficially divergent terms. The auxiliary variables Q_α, $Q_{g_{rr}}$, and $Q_{g_{\theta\theta}}$ are all finite at $r = 0$, but Q_{β^r} diverges.

C. Excision

Eq. (84) (restated below) shows that given a proper choice of the numerical parameter λ, the above Kerr-Schild data will always contain an excision surface at small r inside which all wavespeeds of the system are zero or incoming. If we place an inner boundary of the

computational domain within this excision surface, Sommerfeld boundary conditions reduce to taking the exterior solution equal to the interior solution and on physical grounds no boundary conditions need be imposed. We can therefore freely change our singular domain $\Omega = [0, r_{max}]$ to the domain $[r_{min}, r_{max}]$ with the singularity excised so long as $r_{min} < r_{excision}$, defined to be the largest r satisfying Eq. (84), restated here:

$$\beta^r \geq \max\left(\sqrt{\frac{2\alpha\chi}{g_{rr}}}, \alpha\sqrt{\frac{\chi}{g_{rr}}}, \sqrt{\frac{\lambda}{g_{rr}}}\right). \tag{96}$$

D. Turduckening

The turduckening technique replaces singular black hole data with smooth but constraint violating data. Many choices for this smooth stuffing data are possible, and since the exterior solution is causally disconnected from the turduckened solution in the interior of the horizon the details of the stuffing are unimportant so long as the resulting simulations are stable and robust. Our choices are therefore strongly guided by numerical considerations.

We choose a region $[0, r_t]$ to be turduckened and make the replacement $r \to \overline{r}$ in the equations for the initial data, where the stuffing transformation function $\overline{r}(r)$ is constructed to satisfy the conditions

$$\overline{r}(0) = r_0, \qquad \overline{r}(r_t) = r_t, \qquad \overline{r} = r \quad \text{for} \quad r > r_t. \tag{97}$$

We will further specify that the stuffing transformation $\overline{r}(r)$ has $N_{tur} - 1$ continuous derivatives at $\overline{r}(r_t)$. If we choose $\overline{r}(r)$ to be a polynomial in r inside the turduckened region, this provides a system of $N_{tur} + 1$ linear equations that can be solved for the coefficients of the polynomial.

In effect we are stretching the physically correct (non-singular) data for the region $[r_0, r_t]$ over the whole turduckened region $[0, r_t]$. Initial data turduckened in this manner will naturally be constraint violating on $[0, r_t]$. If the constraints $\mathcal{H}$, $\mathcal{M}$, and $\mathcal{G}$ evolve with wavespeeds that are not superluminal, these violations will not propagate to the outside of the black hole's event horizon. While this is not true in general for BSSN-type systems, evolution equations for the GBSSN constraint system as we have defined it can be calculated and shown to have no superluminal wavespeeds [13], and so we may safely stuff the black hole so long as r_t lies within the event horizon. Despite this result, which formally holds in the limit of the continuum and is rigorously discussed in [14], at finite resolution a numerical scheme may couple the interior and exterior solutions.

As an example of constructing the stuffing transformation $\overline{r}(r)$, consider $N_{tur} = 4$, for which $\overline{r}$ is rigged to satisfy $\overline{r}(r_0) = r_0$, $\overline{r}(r_t) = r_t$, $\overline{r}'(r_t) = 1$, $\overline{r}''(r_t) = 0$, and $\overline{r}'''(r_t) = 0$. This provides a set of linear equations to be solved for the coefficients of the polynomial $C_1 + C_2 r^2 + C_3 r^3 + C_4 r^4 + C_5 r^5$. This particular choice reproduces the polynomial used as turducken stuffing in Eq. (37) of [14]. Note that there is no linear term included in this polynomial. The turduckening procedure can introduce numerical instabilities if the gradient of the transformation is too steep. In this case removing the linear term produces a monotonic polynomial with smaller gradients than the corresponding 4^{th} degree polynomial with $r_0 = 0.1$, $r_t = 0.4$. The polynomials used in the numerical simulations described in Section V use r^5 as the lowest order (non-constant) term to provide a transformation with shallow gradients for $N_{tur} \leq 8$ on the above region.

V. SECOND ORDER SIMULATIONS

This chapter discusses simulations of a turduckened Schwarzschild black hole in spherical symmetry performed with a second order nodal dG scheme. Ref. [23] constructed a nodal dG scheme that led to robustly stable and spectrally convergent black hole simulations with excision, and we demonstrate here that both this robust stability and spectral convergence are maintained when employing turduckening in these simulations. We then present additional results demonstrating that the constraint violations present in turduckened initial data quickly dissipate and that the speed of the constraint decay inside the turduckened region increases with N_{tur}, the degree of smoothness of the stuffing transformation.

A. Code Description

Adopting the conformal Kerr-Schild radial coordinate r described above, the physical domain Ω is taken to be $r = [0, 100]M$. The computational domain Ω_h is defined by splitting this domain into 22 subdomains with the bulk of these subdomains concentrated near $r = 0$ where the field gradients and numerical errors are largest. The first subdomain is also the turduckened region, $\mathsf{D}^1 = [0, r_t] = [0, 0.4]M$. There are then 3 subdomains of equal length covering $[0.4, 1.5M]$, 6 subdomains of equal length covering $[1.5, 10]M$, and 12 subdomains of equal length covering $[10, 100]M$. As described in detail in Section III C, we use a local Lax-Friendrichs flux for the numerical flux coupling the fields between subdomains and choose $C = 2$ in Eq. (87). Since the initial data in Eq. (94) describes a static black hole, the exact solution at all times is given by the (un-turduckened) initial data. This exact solution is used for the outer boundary condition, $W^+ = W_{\text{exact}}$, and since there will always be an excision surface located at some small $r > 0$ we apply no inner boundary conditions and take $W^+ = W^-$ at $r = 0$. This choice of exact outer boundary conditions is unlikely to be generalizable to more complicated dynamic systems, but simulations enforcing Sommerfeld outer boundary conditions were found to be unstable for second order dG GBSSN simulations in [23].

Time integration is performed with a standard fourth order Runge-Kutta method with a timestep Δt chosen for stability. The maximum stable timestep is expected and observed to scale inversely with the maximum wavespeed $\max|\mu(A(u))|$ of the system and with the minimum subdomain size. At each timestep we apply an order $2s = 20$ exponential filter to the top two-thirds of the modal coefficients for each field except g_{rr} and $g_{\theta\theta}$. For stability we observe that g_{rr} and $g_{\theta\theta}$ must not be filtered. A detailed understanding of this is still lacking, though identical behavior is observed in second order excision simulations and in the first order simulations with both excision and turducken discussed below. $\lambda = 0.1$ and $\eta = 50$ are chosen. All simulations are for a unit mass, $M = 1$, schwarzschild black hole with initial data described by Eq. (94). None of these choices are significant departures from the excision scheme presented in [23]. The stability and convergence described below appear robust to variations in filter strength $2s$ and η; similar results are obtained using $\eta = \{0, 10, 20, 50\}$ and $2s = \{6, 10, 20\}$.

To turducken this initial data as described in Section IV D, we choose $r_0 = 0.1M$, $r_t = 0.4M$, and $N_{tur} = 8$. Qualitatively similar results are found with different choices of these parameters. Changing the size of the turduckened region does affect the gradient of the stuffing transformation $\overline{r}(r)$, and the details of the transformation, particularly the order of the lowest non-constant term in the stuffing polynomial, may need to be modified to

account for this and ensure stability for different choices of r_0 and r_t. Varying N_{tur} has a very slight effect on the numerical value of the constraints at late times and a strong effect on the early-time behavior of the constraint violations, as described in detail below. In the simulations described here, r_t is chosen to lie on the boundary of a subdomain, but there are no qualitative differences observed in simulations where this is not the case.

B. Long-term Stability and Convergence

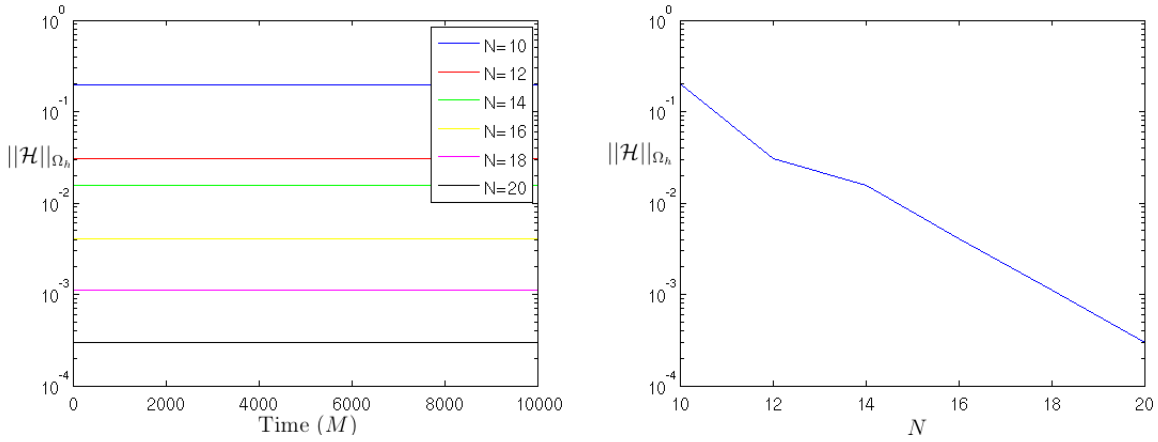

FIG. 3. Stability and spectral convergence of the Hamiltonian constraint. The left plot shows the L_2 norm $||\mathcal{H}||_{\Omega_h}$ as a function of time for simulations with a range of different N. The right plot shows a log scale of the L_2 norm $||\mathcal{H}||_{\Omega_h}$ as measured at $t = 10,000$ in these same six simulations as a function of polynomial order N. For N=10, 12, 14, 16, 18, 20 the timesteps are respectively $\Delta t \approx 0.0043, 0.003, 0.0023, 0.0017, 0.0014, 0.0011$.

The first properties we look to verify for the scheme are stability and accuracy. Binary black hole simulations must run for long times and so the long-term stability of our model simulations is essential. The turduckened simulations in this section can be run to time $t = 10,000M$ with no growth in numerical error appearing. One of the most important benefits of a dG scheme is its spectral convergence, so it is especially important that we verify that the numerical error in our simulations does decrease exponentially when we increase N, the order of the interpolating polynomials used to approximate the evolved fields. This has been shown to hold for second order GBSSN simulations using excision in [23], and so our first major result is to show that these turduckened simulations still possess spectral convergence.

The main tool for monitoring the accuracy of our simulations is checking that the Hamiltonian, momentum, and conformal connection constraints given in Eq. (45) hold at all times. We observe that the Hamiltonian constraint is the first to diverge when numerical instabilities begin to develop, and so monitoring $\mathcal{H}$ provides a measure of the overall accuracy of the simulation that is sensitive to numerical instabilities. The errors in the fields themselves have been observed to share the same convergence properties as those shown for the Hamiltonian constraint, that is we observe that for example $||(g_{rr})_{\rm num} - (g_{rr})_{\rm analytic}|| \to 0$ so long as $||\mathcal{H}|| \to 0$. Furthermore, since the constraint violations inside the turduckened region quickly shrink, as is discussed below, there is no significant difference between the

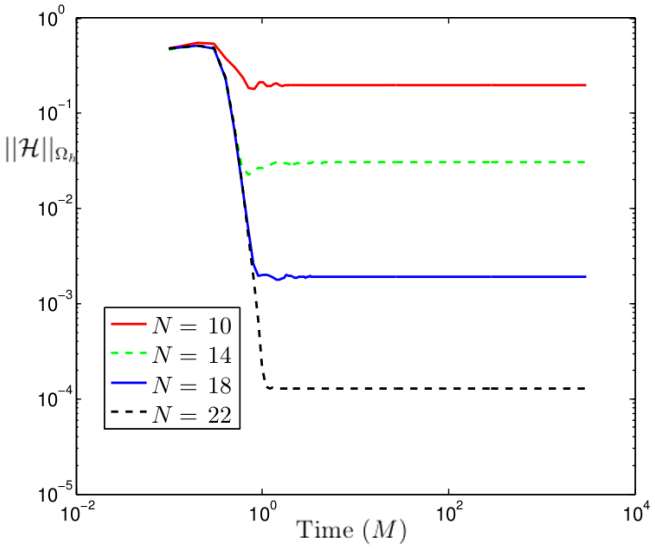

FIG. 4. Rapid decay in the Hamiltonian constraint at early times. This plot shows a log-scale of the L_2 norm $||\mathcal{H}||_{\Omega_h}$ as a function of log-scale time for a range of polynomial degrees N.

L_2 norm over the entire domain and the norm taken with the turduckened region excluded, and so we simply monitor $||\mathcal{H}||_{\Omega_h}$.

The long-term stability and spectral convergence of our turduckened dG scheme are shown in Fig. 3. As with second order excision simulations, there is no observed growth in $||\mathcal{H}||_{\Omega_h}$ over long times and the constraint violations measured at late times decrease exponentially with N. The magnitude of $||\mathcal{H}||_{\Omega_h}$ for a given value of N shown is orders of magnitude larger than the corresponding value measured in the excision simulations of [23], but the rate of convergence appears qualitatively similar to the excision case. At high resolutions there are no significant differences in the value of $||\mathcal{H}||_{\Omega_h}$ throughout the domain between turduckened and excision simulations after very early times. With $N = 40$ for example, the L_2 norm $||\mathcal{H}||_{\Omega_h}$ is actually almost 25% lower at $t = 10M$ in turduckened simulations then in excision simulations with the same timestep and numerical parameters and an r-coordinate domain of $[0.4, 100]M$ with a subdomain structure identical to that described above for this region.

C. Further Results on Turduckening

1. *Constraint Propagation*

Since the turduckened fields in the initial data do not satisfy the constraints, $||\mathcal{H}||_{\Omega_h}$ is typically of order 1 at $t = 0$ and independent of N. This resolution independence is reasonable, as the constraint violations in the rest of the domain are orders of magnitude smaller than the violations due to the turduckening at all resolutions considered, and so the overall L_2 norm will depend only on the size of the turduckened region relative to the full domain. It is observed in turduckened finite difference simulations that these initial constraint violations quickly dissipate, and by time $t = 10M$ the interior solution has settled into a non-singular steady-state solution that satisfies the GBSSN constraints up to violations of

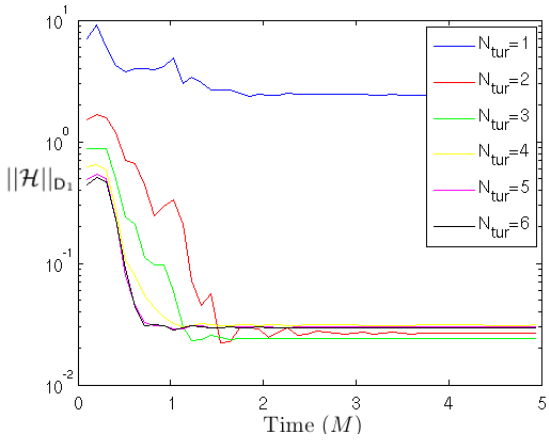

FIG. 5. Early time behavior of the Hamiltonian constraint inside the turduckened region with various choices of N_{tur}. This plot shows the L_2 norm $||H||_{\mathrm{D}^1}$ for the Hamiltonian constraint in the turduckened region $0 \leq r \leq r_t = 0.4M$ for times up to $t = 5M$. Each line corresponds to a different degree of smoothness N_{tur} of the turduckened data at r_t, where $N_{tur} = 1$ corresponds to continuous data, $N_{tur} = 2$ corresponds to a continuous first derivative $\overline{r}'(r)$, etc. All simulations shown in this plot are for $N = 12$.

the same order of magnitude as the exterior solution [14]. The mechanism proposed for this in [14] is that the constraint violations propagate causally but the radial coordinate itself has a superluminal velocity and so the coordinate region of constraint violation rapidly shrinks. Similar dissipation is observed in our simulations, and at high resolution the value of the constraint violations even at the $r = 0$ grid point drops to the same order of magnitude as the constraint violations throughout the rest of the domain by $t = 4M$. Fig. 4 demonstrates this rapid decay in $||\mathcal{H}||$ averaged throughout the whole domain at early times as well as late-time stability and convergence.

2. Dependence on Smoothness of Initial Data

The early-time decay of $||\mathcal{H}||_{\mathrm{D}^1}$, the L_2 norm of the Hamiltonian constraint inside the turduckened region, is observed to depend on N_{tur}, the degree of smoothness of the stuffing transformation $\overline{r}(r)$ at the interface r_t. This is demonstrated in Fig. 5, which shows the early times of simulations with $N = 12$ and various N_{tur}. So long as the stuffing transformation is at least differentiable ($N_{tur} = 2$) the constraint violations do quickly decay inside the turduckened region, with higher values of N_{tur} corresponding to faster decay. There is a slight but non-zero difference in the steady-state value of the constraint violations reached inside the turduckened region, but this effect is not significant and has no clear relationship to N_{tur}.

VI. FIRST ORDER SIMULATIONS

In this chapter we present a first order reduction of the GBSSN system we will refer to as FOBSSN and perform simulations of a black hole in spherical symmetry using the FOBSSN

system. We find that FOBSSN simulations using excision are stable and spectrally accurate when using exact boundary conditions, and unlike second order GBSSN simulations are stable and spectrally accurate with Sommerfeld outer boundary conditions. We have been unable to achieve robustly stable FOBSSN simulations using turduckening. All simulation results in this chapter were previously published in [11], but the surrounding discussion has been heavily modified to follow the notation and scope of this thesis and in particular this is the first explicit appearance of the evolution equations for the GBSSN auxiliary variables.

A. Auxiliary Variables and Constraints

To perform the first order reduction we promote the auxiliary fields to be evolved variables rather than local variables calculated at each timestep. The necessary axillary fields for our simulations in spherical symmetry are

$$Q_\alpha \equiv \partial_r \alpha, \qquad Q_{\beta^r} \equiv \partial_r \beta^r, \qquad Q_\chi \equiv \partial_r \chi, \qquad Q_{g_{rr}} \equiv \partial_r g_{rr}, \qquad Q_{g_{\theta\theta}} \equiv \partial_r g_{\theta\theta}. \tag{98}$$

Note that the number of axillary variables that must be defined is greatly increased when working in full three-dimensional Cartesian coordinates. The definitions of the axillary fields introduce new associated constraints for the FOBSSN system:

$$\mathcal{A}_r \equiv Q_\alpha - \partial_r \alpha = 0 \tag{99a}$$
$$\mathcal{B}^r_r \equiv Q_{\beta^r} - \beta^r = 0 \tag{99b}$$
$$\mathcal{C}_r \equiv Q_\chi - \partial_r \chi \tag{99c}$$
$$\mathcal{D}_{rrr} \equiv Q_{g_{rr}} - \partial_r g_{rr} \tag{99d}$$
$$\mathcal{D}_{\theta\theta r} \equiv Q_{g_{\theta\theta}} - \partial_r g_{\theta\theta}. \tag{99e}$$

The presence of these auxiliary constraints presents a genuine difference between the GBSSN and FOBSSN systems that is especially relevant to the construction of a turduckened FOBSSN scheme. In particular, recall that in the second order scheme these constraints define residuals used to enforce Galerkin conditions that define the auxiliary variables at each timestep. With FOBSSN the auxiliary variables are calculated according to their own discretized evolution equations (also recall we use a local Lax-Friendrichs flux for f^*_Q instead of the penalized central flux used in the second order scheme), so these constraints are no longer explicitly enforced in the numerical scheme.

The GBSSN system is trivially modified to be in the proper form for FOBSSN evolution and constraint equations by replacing $u' \to Q$ and $u'' \to Q'$. The evolution equations for the auxiliary variables can be found simply by taking a spatial derivative of the evolution equations for the corresponding field and using the commutativity of mixed partials and are

given by

$$\partial_t Q_\alpha = Q_{\beta^r} Q_\alpha + \beta^r Q'_\alpha - 2 Q_\alpha K - 2\alpha K' - \kappa^\alpha \mathcal{A}_r \tag{100a}$$

$$\partial_t Q_{\beta^r} = Q^2_{\beta^r} + \beta^r Q'_{\beta^r} + \frac{3}{4} B^{r\prime} - \kappa^\beta \mathcal{B}^r_r \tag{100b}$$

$$\begin{aligned}\partial_t Q_\chi =& Q_{\beta^r} Q_\chi + \beta^r Q'_\chi + \frac{2}{3} K' \alpha \chi + \frac{2}{3} K Q_\alpha \chi + \frac{2}{3} K \alpha Q_\chi - \frac{Q_{\beta^r} Q_{g_{rr}} \chi}{3 g_{rr}} - \frac{\beta^r Q_{g'_{rr}} \chi}{3 g_{rr}} \\ & - \frac{\beta^r Q_{g_{rr}} Q_\chi}{3 g_{rr}} + \frac{\beta^r Q^2_{g_{rr}} \chi}{3 g^2_{rr}} - \frac{2}{3} Q'_{\beta^r} \chi - \frac{2}{3} Q_{\beta^r} Q_\chi - \kappa^\chi \mathcal{C}_r\end{aligned} \tag{100c}$$

$$\begin{aligned}\partial_t Q_{g_{rr}} =& \frac{2}{3} Q_{\beta^r} Q_{g_{rr}} + \frac{2}{3} \beta^r Q'_{g_{rr}} + \frac{4}{3} Q_{g_{rr}} Q_{\beta^r} + \frac{4}{3} g_{rr} Q'_{\beta^r} - 2 A'_{rr} \alpha - 2 A_{rr} Q_\alpha \\ & - \frac{2 Q_{g_{rr}} \beta^r Q_{g_{\theta\theta}}}{3 g_{\theta\theta}} - \frac{2 g_{rr} Q_{\beta^r} Q_{g_{\theta\theta}}}{3 g_{\theta\theta}} - \frac{2 g_{rr} \beta^r Q'_{g_{\theta\theta}}}{3 g_{\theta\theta}} + \frac{2 g_{rr} \beta^r Q^2_{g_{\theta\theta}}}{3 g^2_{\theta\theta}} - \kappa^g \mathcal{D}_{rrr}\end{aligned} \tag{100d}$$

$$\begin{aligned}\partial_t Q_{g_{\theta\theta}} =& \frac{1}{3} Q_{\beta^r} Q_{g_{rr}} + \frac{1}{3} \beta^r Q'_{g_{\theta\theta}} + \frac{A'_{rr} g_{\theta\theta} \alpha}{g_{rr}} + \frac{A_{rr} Q_{g_{\theta\theta}} \alpha}{g_{rr}} + \frac{A_{rr} g_{\theta\theta} Q_\alpha}{g_{rr}} - \frac{A_{rr} g_{\theta\theta} \alpha Q_{g_{rr}}}{g^2_{rr}} \\ & - \frac{Q_{g_{\theta\theta}} \beta^r Q_{g_{rr}}}{3 g_{rr}} - \frac{g_{\theta\theta} Q_{\beta^r} Q_{g_{rr}}}{3 g_{rr}} - \frac{g_{\theta\theta} \beta^r Q'_{g_{rr}}}{3 g_{rr}} + \frac{g_{\theta\theta} \beta^r Q^2_{g_{rr}}}{3 g^2_{rr}} - \frac{2}{3} Q_{g_{\theta\theta}} Q_{\beta^r} \\ & - \frac{2}{3} g_{\theta\theta} Q_{\beta^r} - \kappa^g \mathcal{D}_{\theta\theta r}.\end{aligned} \tag{100e}$$

Note that we have also introduced terms proportional to the auxillary constraints in each evolution equation. These are trivially zero in the continuum limit and so can be added freely. The parameters κ^α, κ^β, κ^χ and κ^g are chosen for numerical stability and allow for damping of the axillary constraints. Evolution equations for the auxiliary constraints, found by taking the time derivative of Eq. (99), are given by simply replacing each auxiliary variable in Eq. (100) with the corresponding constraint. These equations for the evolution of each constraint therefore feature the corresponding damping parameter κ in each equation, and so setting these damping parameters to a sufficiently large value will indeed damp the auxiliary constraints.

B. Excision Results

To isolate the effects of turduckening from those of using the first order scheme more generally, we first consider dG simulations of the FOBSSN system using excision. The computational domain is taken to be $r = [0.4, 50]M$ and for simplicity is divided into 100 equally spaced subdomains. We use a local Lax-Friendrichs flux for all evolved fields, including the auxiliary variables, and as before choose $C = 2$, $\lambda = 0.1$, and $\eta = 50$ and take a unit mass, $M = 1$, schwarzschild black hole constructed in Kerr-Schild coordinates according to Eq. (94) as initial data. We apply an exponential filter of strength $2s = 20$ to all fields except g_{rr} and $g_{\theta\theta}$, including the auxiliary variables, and choose the timestep Δt for stability. The auxiliary damping parameters are chosen as $\kappa^\alpha = \kappa^\beta = \kappa^\chi = \kappa^g = 20$.

Using exact outer boundary condition allows for long-term stable simulations with spectral convergence of the constraints, as with the second order scheme. In contrast with the second order scheme, enforcing Sommerfeld outer boundary conditions also allows for stable FOBSSN simulations. Fig. 6 demonstrates the long-term stability and spectral convergence of the FOBSSN scheme with Sommerfeld boundary conditions. In an attempt to remove the

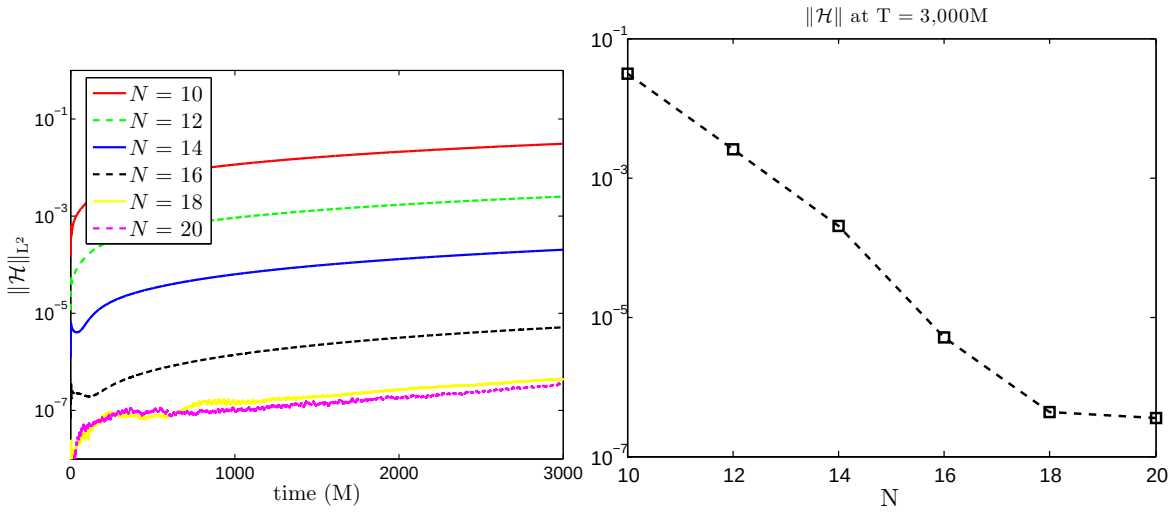

FIG. 6. Stability and convergence of the Hamiltonian constraint with Sommerfeld boundary conditions. The left plot shows the L_2 norm $||\mathcal{H}||_{\Omega_h}$ as a log-scale function of time for simulations run to $t = 3,000M$ at varying resolutions. The right plot shows log-scale $||\mathcal{H}||_{\Omega_h}$ as measured at $t = 3,000M$ in these same simulations as a function of N. The highest two resolutions have essentially reached double precision roundoff errors.

slow growth of the Hamiltonian constraint in time visible in this figure, we varied our numerical setup including the exponential filter parameters (the number of filtered modes, the dissipation exponent, and which variables to filter), the timestep, the B^r damping parameter η, the numerical flux dissipation parameter, and the auxiliary field damping parameters without significant improvements.

C. Turduckening Results

As described in Chapter V, turduckening was straightforwardly incorporated into the second order GBSSN scheme and allowed for robustly stable simulations with no need for fine-tuning the numerical setup. This is not the case with the FOBSSN system. The definition of the auxiliary fields creates an ambiguity in how to turducken to FOBSSN initial data, since for example $Q_\alpha(\bar{r}) \neq \partial_r \alpha(\bar{r})$. This creates two distinct natural choices for defining turduckened auxiliary variables: 1-take the derivatives of the u sector variables analytically and compute their values at the turduckened grid points to calculate $Q_\alpha(\bar{r})$ or 2-apply the numerical derivative operator to the turduckened u sector variables to calculate $\partial_r \alpha(\bar{r})$. With the first choice the auxiliary constraints are violated in the initial data, while with the second choice the auxiliary constraints are satisfied but the turduckened initial data no longer represents the physically correct data for $[r_0, r_t]$ stretched over the region $[0, r_t]$. We experimented with both choices and found that the region of constraint violations no longer shrinks when using the first choice of data that violates the auxiliary constraints. A comparison in the constraint behavior of the system with both choices at early times is shown in Fig. 7.

We have been unable to achieve long-term stable turduckened simulations using either choice. A typical evolution with either choice lasts on the order of tens of M to hundreds of

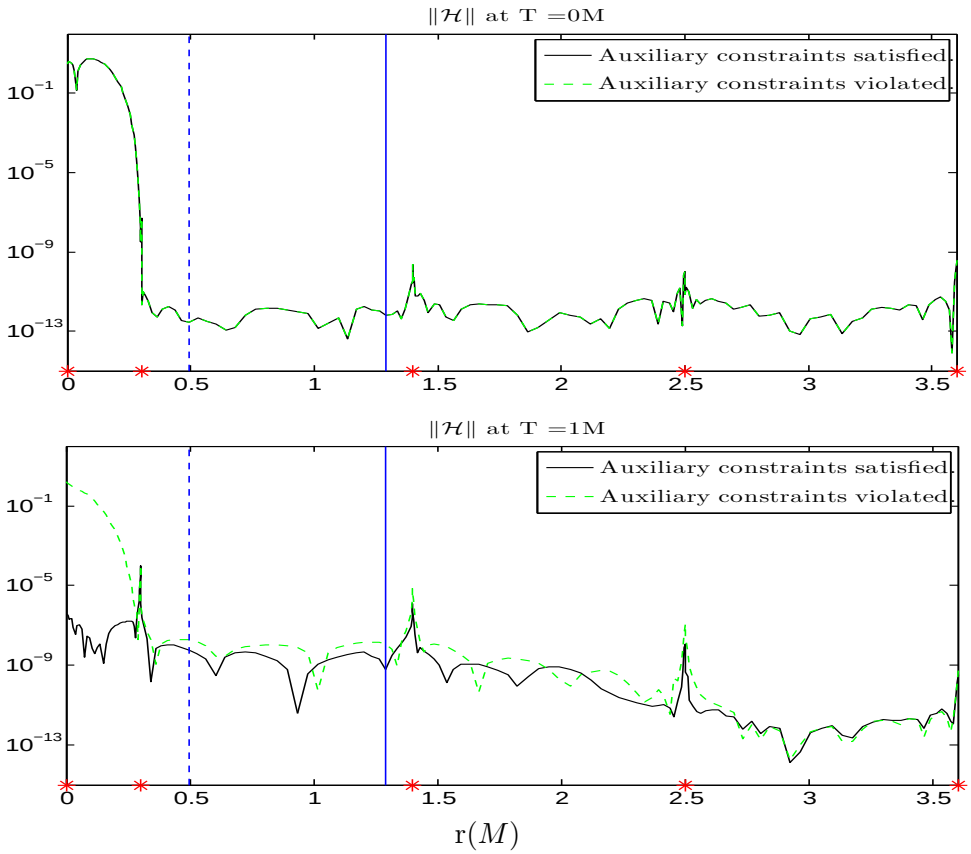

FIG. 7. Snapshots of the Hamiltonian constraint for turduckened FOBSSN data which satisfies (black line) and violates (dashed green line) the auxiliary constraints given in Eq. (99). The top plot shows the L_2 norm $||\mathcal{H}||_{\Omega_h}$ at $t = 0$ and the bottom plot shows this same norm at $t = 1M$. Notice that only in the case where the auxiliary constraints are satisfied by the turduckened fields does the region of constraint violation shrink during this time. The solid vertical line marks the location of the event horizon, and the dashed line marks the location of the excision surface. The large red asterisks on the horizontal axis mark the location of each subdomain boundary. The turduckened region is specified by $r_0 = 0.1M$ and $r_t = 0.3M$, also the boundary of the first subdomain.

M, though some simulations with finely tuned choices of numerical parameters can last into the thousands of M at lower resolution. Stability is not observed to increase with increasing resolution. Though the second choice of turduckened data that satisfies the auxiliary constraints uniquely leads to a decay of the Hamiltonian constraint in the turduckened region, neither choice provides a clear advantage over the other in long-term stability.

VII. SCALAR FIELD SIMULATIONS

The simulations presented so far have all been limited to evolving vacuum spacetimes. In this chapter we consider coupling a simple and extensively studied matter system, namely a massless scalar field, to the GBSSN system and perform some basic simulations to verify that dG methods can be used to straightforwardly construct a stable scheme for solving the

coupled system. After giving a brief introduction to the problem of simulating strongly gravitating matter systems in Section A, we derive the necessary constructions for incorporating a massless scalar field into our GBSSN simulations: evolution equations for the scalar field with gravitational contributions written in terms of the GBSSN variables, the GBSSN matter source terms for the scalar field, characteristics and boundary conditions for the matter system, and initial data for the scalar field. Section C presents some preliminary simulation results: the matter system is robustly stable and spectrally accurate when evolved in flat space and fully coupled simulations of a scalar pulse falling into a Kerr-Schild black hole are robustly stable and result in radiation scattering off the black hole whose amplitude decays as a power law in late times.

A. Overview

There are many strongly gravitating systems worth studying other than black holes. Even within the context of gravitational wave detection, there are efforts underway to study the gravitational radiation emitted from the merger of two neutron stars through numerical simulations [42]. In order to perform simulations of neutron stars, core-collapse supernovae, accretion flows, or other systems interesting to high-energy astrophysics or gravitational wave astronomy we must solve the equations of GR in the presence of matter described by a non-zero stress-energy tensor.

Solving BSSN or other GR formulations in the presence of matter is often complicated by the presence of shocks in the solution. Spectral methods are generally very sensitive to the presence of shocks, and even state-of-the-art codes for spectral gravity evolution use a separate finite-difference grid for evolving matter fields in neutron star simulations [34, 42]. DG methods are an exception to this rule and are particularly well-suited to sharply resolving shocks in solutions while maintaining spectral accuracy in evolving smooth pieces of the solution. An example of this ability to manage shocks in the context of relativity is given by [43], in which a dG scheme for general relativistic hydrodynamics is constructed and a one-dimensional model code is shown to robustly pass several tests of its capabilities for stably evolving shocks.

To the best of our knowledge, there have been no simulations constructed that evolve a BSSN-type system in the presence of matter fields using dG methods. In this chapter we will present simulations of a very simple matter system: a massless scalar field in a spherically symmetric spacetime. With these simulations we look to demonstrate that our dG scheme can straightforwardly evolve a system with a dynamic matter field coupled to the GBSSN system without requiring the introduction of any new numerical tricks to achieve robust stability. Massless scalar fields have been studied extensively in other numerical simulations, especially in the context of gravitational collapse, see [26] for a review and [24] for simulations using the GBSSN system, and infall into a black hole. Gravitational collapse is difficult to model in spherical coordinates since before the collapse there is no inner excision surface and suitable boundary conditions must be enforced at the inner boundary. Successful gravitational collapse simulations required imposing additional regularity conditions at the origin [39] and sometimes employ at least one null coordinate instead of the spherical coordinates used here [16, 19]. Since the difficulty of finding proper conditions for stability at the origin is not present in three-dimensional Cartesian coordinate simulations and is a feature of using spherical coordinates rather than a general feature of evolving matter systems, we will avoid this difficulty and limit ourselves to the study of systems possessing

an inner excision surface at all times.

A simple scenario possessing such an excision surface is the infall of a localized pulse of scalar field matter into a black hole. For simplicity we will employ the Kerr-Schild initial data used in our previous simulations and limit ourselves sufficiently small pulses whose gravitational effects can be treated as perturbations of this black hole spacetime rather than undertake the construction of initial data that satisfies the GBSSN constraints for a black hole in the presence of matter. This simple scenario still possesses interesting physics, and numerous simulations of black holes perturbed by scalar fields show that in general circumstances as the black hole relaxes from a perturbed state back to its stationary ("no hair") state it emits scalar radiation whose amplitude decays as a power-law at late times as it scatters off spacetime curvature [2, 5, 6, 30].

B. Scheme for Simulating a Massless Scalar Field

1. First Order Evolution Equations

Throughout this chapter we will consider a scalar field $\varphi(t, x)$ that satisfies the massless Klein-Gordon equation (the source-free covariant wave equation):

$$\Box\varphi \equiv \nabla_\mu \nabla^\mu \varphi = 0 \tag{101}$$

To find the gravitational coupling of this field in terms of our evolved GBSSN variables, we can use the fact that $\sqrt{-\overline{g}}$ [5] is a scalar density of weight +1 and an identity $\nabla_\mu \sqrt{-\overline{g}} = 0$ derived from metric compatibility [20] to derive a useful identity for the Klein-Gordon equation:

$$\begin{aligned} \Box\varphi &= \tfrac{1}{\sqrt{-\overline{g}}} \nabla_\mu \left(\sqrt{-\overline{g}} \partial^\mu \varphi \right) = \tfrac{1}{\sqrt{-\overline{g}}} \partial_\mu \left(\sqrt{-\overline{g}} \partial^\mu \varphi \right) \\ &= \tfrac{1}{\sqrt{-\overline{g}}} \partial_\mu \left(\sqrt{-\overline{g}}\, \overline{g}^{\mu\nu} \partial_\nu \varphi \right). \end{aligned} \tag{102}$$

Using this form of the Klein-Gordon equation and our definitions for the metric components in Eq. 7 [6], we can express the Klein-Gordon equation for φ as

$$\begin{aligned} \sqrt{-\overline{g}} \Box\varphi &= \partial_t \left(\sqrt{-\overline{g}}\, \overline{g}^{tt} \partial_t \varphi + \sqrt{-\overline{g}}\, \overline{g}^{tr} \partial_r \varphi \right) + \partial_r \left(\sqrt{-\overline{g}}\, \overline{g}^{tr} \partial_t \varphi + \sqrt{-\overline{g}}\, \overline{g}^{rr} \partial_r \varphi \right) \\ &= \partial_t \left[\alpha^{-2} \sqrt{-\overline{g}} \left(-\partial_t \varphi + \beta^r \partial_r \varphi \right) \right] + \partial_r \left[\alpha^{-2} \sqrt{-\overline{g}} \beta^r \left(\partial_t \varphi - \beta^r \partial_r \varphi \right) + \sqrt{-\overline{g}}\, \gamma^{rr} \partial_r \varphi \right]. \end{aligned} \tag{103}$$

The determinant of the physical metric is simply related to the determinant of the spatial metric by $\overline{g} = -\alpha^2 \gamma$. This allows us to express $\sqrt{-g}$ in terms of our evolved GBSSN variables as

$$\sqrt{-\overline{g}} = \alpha \sqrt{\gamma} = \alpha \chi^{-3/2} \sqrt{g} = \alpha \chi^{-3/2} \sqrt{g_{rr}} g_{\theta\theta} \sin\theta. \tag{104}$$

---

[5] Remember that $\overline{g}_{\mu\nu}$ is the physical spacetime metric, $\gamma_{\mu\nu}$ is the spatial piece of the physical metric, and the notation $g_{\mu\nu}$ is reserved for the conformal spatial metric defined by $g_{\mu\nu} \equiv \chi \gamma_{\mu\nu}$.

[6] In the spherically symmetric reduction we have in particular $\overline{g}^{tt} = -\alpha^{-2}$, $\overline{g}^{tr} = \alpha^{-2}\beta^r$, and $\overline{g}^{rr} = \gamma^{rr} - \alpha^{-2}(\beta^r)^2$

To recast Eq. (103) as a first order PDE, as is commonly done in simulations of scalar fields in numerical relativity [29], we introduce the following variables:

$$\Phi \equiv \partial_r \varphi \tag{105a}$$

$$\Pi \equiv \alpha^{-2}\sqrt{-\overline{g}}(\partial_t \varphi - \beta^r \partial_r \varphi)(\sin\theta)^{-1} = \frac{\sqrt{g_{rr}}g_{\theta\theta}}{\alpha\chi^{3/2}}(\partial_t \varphi - \beta^r \partial_r \varphi). \tag{105b}$$

Remembering that the normal vector for our foliation of spacelike hypersurfaces in Chapter II is given by $n^\mu = \alpha^{-1}(1, -\beta^i)$, Π is actually just the derivative normal to the spacelike hypersurfaces weighted by $\sqrt{-\overline{g}}$. We will use Φ and Π as the evolved variables for simulations of the scalar field φ. Their evolution equations are found by applying commutativity of mixed partials ($\partial_t \Phi = \partial_r \partial_t \varphi$) and Eq. (103):

$$\partial_t \varphi = \beta^r \Phi + \frac{\alpha\chi^{3/2}}{\sqrt{g_{rr}}g_{\theta\theta}}\Pi \tag{106a}$$

$$\partial_t \Phi = \partial_r \left(\beta^r \Phi + \frac{\alpha\chi^{3/2}}{\sqrt{g_{rr}}g_{\theta\theta}}\Pi\right) \tag{106b}$$

$$\partial_t \Pi = \partial_r \left(\frac{\alpha g_{\theta\theta}}{\sqrt{\chi g_{rr}}}\Phi + \beta^r \Pi\right). \tag{106c}$$

2. Stress-Energy Tensor and Source Terms

The above equations allow us to evolve the scalar field in the presence of a curved spacetime background. To fully describe the system we must also determine how coupling the scalar field φ to that spacetime background affects the geometry. The GBSSN system presented in Eqs. (44), (45) is valid for a spacetime with an arbitrary collection of matter described by a stress-energy tensor $T^{\mu\nu}$. Describing the response of the GBSSN variables to the scalar field therefore amounts to determining the stress-energy tensor for φ and in particular the matter variables ρ, S, S^{TF}_{rr}, and j^r defined at the end of Section II C that are featured in the GBSSN system.

The Lagrangian for our scalar field is given by $\mathcal{L}_{\rm M} = -\frac{1}{2}\nabla_\mu \varphi \nabla^\mu \varphi$, as may be verified by varying the action

$$S_M = \int d^4x\, \mathcal{L}_{\rm M} = \int d^4x \left[-\frac{1}{2}\nabla_\mu \varphi \nabla^\mu \varphi\right]. \tag{107}$$

After a few integrations by parts where we ignore boundary terms (we assume $\varphi(\pm\infty) \to 0$) this variation gives $\delta S_M = (\nabla_\mu \nabla^\mu \varphi)\delta\varphi = 0$, and so the Klein-Gordon equation is recovered as the equation of motion for φ. With the action in general relativity expressed in the form

$$S = \int d^4x \left[\frac{1}{16\pi G}\mathcal{L}_G + \mathcal{L}_M\right]\sqrt{-\overline{g}}, \tag{108}$$

the Einstein field equations are recovered by demanding that the variation $\frac{\delta S}{\delta g^{\mu\nu}}$ vanish. To recover the non-vacuum Einstein field equations the stress-energy tensor must be related to this action by $T_{\mu\nu} = \frac{-2}{\sqrt{-\overline{g}}}\frac{\delta \mathcal{L}_{\mathcal{M}}}{\delta g^{\mu\nu}}$. Carrying out this variation even for the simple scalar field Lagrangian is still a non-trivial calculation and we will not work it out explicitly. The result is given by [18]

$$T_{\mu\nu} \equiv \frac{-2}{\sqrt{-\overline{g}}}\frac{\delta \mathcal{L}_{\mathcal{M}}}{\delta g^{\mu\nu}} = \nabla_\mu \varphi \nabla_\nu \varphi - \frac{1}{2}\overline{g}_{\mu\nu}\overline{g}^{\rho\sigma}\nabla_\rho \varphi \nabla_\sigma \varphi. \tag{109}$$

This can be expressed in terms of the GBSSN variables and the matter variables φ, Φ, and Π as

$$\begin{aligned} T_{\mu\nu} &= \partial_\mu\varphi\partial_\nu\varphi - \frac{1}{2}\overline{g}_{\mu\nu}\left[\alpha^{-2}(-(\partial_t\varphi)^2 + 2\beta^r\partial_t\varphi - (\beta^r\partial_r\varphi)^2) + \gamma^{rr}(\partial_r\varphi)^2\right] \\ &= \partial_\mu\varphi\partial_\nu\varphi + \frac{1}{2}\overline{g}_{\mu\nu}\left(-\frac{\chi}{g_{rr}}\Phi^2 + \frac{\chi^3}{g_{rr}g_{\theta\theta}^2}\Pi^2\right). \end{aligned} \tag{110}$$

The matter variables ρ, S, $S_{rr}^{\rm TF}$, and j^r appear as source terms in the GBSSN evolution equations, and ρ and j^r further specify the proper value of the Hamiltonian and momentum constraints are related to the components of the stress-energy tensor and the GBSSN variables by

$$\rho \equiv n^\mu n^\nu T_{\mu\nu} = \alpha^{-2}\left(T_{tt} - 2\beta^r T_{tr} + (\beta^r)^2 T_{rr}\right) \tag{111a}$$

$$S \equiv {\rm Tr}S_{ij} = {\rm Tr}T_{ij} = \frac{\chi}{g_{rr}}T_{rr} + \frac{2\chi}{g_{\theta\theta}}T_{\theta\theta} \tag{111b}$$

$$S_{rr}^{\rm TF} \equiv T_{rr} - \frac{1}{3\chi}S g_{rr} \tag{111c}$$

$$j^r \equiv (-\gamma^{r\mu}n^\nu T_{\mu\nu}) = \frac{\chi}{\alpha g_{rr}}\left(\beta^r T_{rr} - T_{tr}\right) \tag{111d}$$

There is little insight gained from substituting Eq. (110) into Eq. (111) to express these source terms in terms of the evolved matter variables, and in the simulations to follow we simply perform this substitution numerically.

3. Boundary Conditions

The evolution equation for φ features a zero principle part, and so we can specify $f_\varphi^* = f_\varphi = 0$ just as we specified $f_u^* = f_u = 0$ when considering the abstract GBSSN system. We therefore do not need to apply any boundary conditions to φ. The evolution equations for Φ and Π feature zero source terms, and so Sommerfeld boundary conditions are a natural choice. These can be derived by considering the characteristic variables and wavespeeds of the evolution equations as in the construction sketched in Section III C. Since we are now working with a far simpler system than the GBSSN equations we will perform the construction for the first order Klein-Gordon system in detail. We begin by writing the evolution system for Φ and Π as a matrix equation analogous to the abstract GBSSN system in Eq. (79) as

$$\partial_t\begin{pmatrix}\Phi\\ \Pi\end{pmatrix} + B(u)\,\partial_r\begin{pmatrix}\Phi\\ \Pi\end{pmatrix} \equiv \partial_t\begin{pmatrix}\Phi\\ \Pi\end{pmatrix} + \begin{pmatrix}-\beta^r & -\frac{\alpha\chi^{3/2}}{\sqrt{g_{rr}}g_{\theta\theta}}\\ -\frac{\alpha g_{\theta\theta}}{\sqrt{\chi g_{rr}}} & -\beta^r\end{pmatrix}\partial_r\begin{pmatrix}\Phi\\ \Pi\end{pmatrix} = 0. \tag{112}$$

The matrix $B(u)$ is diagonalizable with eigenvalues are given by

$$\mu^\pm = -\beta^r \pm \alpha\sqrt{\frac{\chi}{g_{rr}}}. \tag{113}$$

These define the wavespeeds of the matter evolution system. Note that they match the wavespeeds $\mu_5^\pm$ of the GBSSN system given in Eq. (80). This simplifies the numerics of

scalar field simulations since adding the matter evolution equations to the GBSSN system does not introduce any new distinct wavespeeds that could impact the existence or location of an excision surface or force a change in our choice of stable timestep.

The corresponding eigenvectors of the matrix $B(u)$ are given by $\left(\begin{smallmatrix} g_{\theta\theta}/\chi \\ 1 \end{smallmatrix}\right)$ and $\left(\begin{smallmatrix} -g_{\theta\theta}/\chi \\ 1 \end{smallmatrix}\right)$. The matter evolution system can therefore be expressed as

$$\partial_t \begin{pmatrix} \Phi \\ \Pi \end{pmatrix} + \frac{1}{2} \begin{pmatrix} \frac{g_{\theta\theta}}{\chi} & -\frac{g_{\theta\theta}}{\chi} \\ 1 & 1 \end{pmatrix} \begin{pmatrix} \mu^- & 0 \\ 0 & \mu^+ \end{pmatrix} \begin{pmatrix} \frac{\chi}{g_{\theta\theta}} & 1 \\ -\frac{\chi}{g_{\theta\theta}} & 1 \end{pmatrix} \partial_r \begin{pmatrix} \Phi \\ \Pi \end{pmatrix} = 0. \tag{114}$$

The characteristic fields are given by applying the matrix $U \equiv \left(\begin{smallmatrix} \frac{\chi}{g_{\theta\theta}} & 1 \\ -\frac{\chi}{g_{\theta\theta}} & 1 \end{smallmatrix}\right)$ to our system vector $Y \equiv \left(\begin{smallmatrix} \Phi \\ \Pi \end{smallmatrix}\right)$ in order to transform the system into the eigenbasis of $B(u)$. This provides us with the incoming and outgoing solutions X^- and X^+[7],

$$\begin{pmatrix} X^- \\ X^+ \end{pmatrix} \equiv U \begin{pmatrix} \Phi \\ \Pi \end{pmatrix} = \begin{pmatrix} \frac{g_{\theta\theta}}{\chi}\Phi + \Pi \\ -\frac{g_{\theta\theta}}{\chi}\Phi + \Pi \end{pmatrix}. \tag{115}$$

Remember that in a dG scheme coupling between subdomains occurs through the numerical flux and so boundary conditions are imposed by specifying the external solution Y^+ to be used in calculated the numerical flux in the boundary subdomain. At the outermost subdomain D^K we wish to enforce a Sommerfeld boundary condition, that is the external solution Y_K^+ should have zero incoming characteristics and should match the outgoing characteristics of the numerical solution Y_K^-. The above relation between the characteristic variables and the matter evolution system variables can be used to express this condition as a system of linear equations for the external fields Φ_K^+ and Π_K^+ in terms of the internal fields Φ_K^- and Π_K^-:

$$X^-(Y_K^+) = \frac{g_{\theta\theta}}{\chi}\Phi_K^+ + \Pi_K^+ = 0 \tag{116a}$$

$$X^+(Y_K^+) = -\frac{g_{\theta\theta}}{\chi}\Phi_K^+ + \Pi_K^+ = X^+(Y_K^-) = -\frac{g_{\theta\theta}}{\chi}\Phi_K^- + \Pi_K^-. \tag{116b}$$

As a brief aside, note that there is an apparent ambiguity in choosing the values of the GBSSN variables used to calculate $X^+(Y_K^+)$. This ambiguity is resolved by noting that only the variables in the u sector of the GBSSN system are present. Due to the presence of the auxiliary sector Q we take $f_u = f_u^* = 0$ and apply no boundary conditions to the u sector. This is equivalent to $u^+ = u^-$ at the boundary, and so we can safely use u^-, the GBSSN variables of the numerical solution, when calculating all the characteristic variables $X^\pm(Y_K^\pm)$. A similar situation occurs when calculating Sommerfeld boundary conditions for the GBSSN system since the matrix $A(u)$ depends on this same sector. With this resolved,

[7] Due to an unfortunate coincidence of notation it is standard to denote both incoming/outgoing solutions and the interior/exterior solutions to a subdomain in dG with $\pm$. The characteristic variables X^+ and X^- will always denote the outgoing (traveling from small r to large r) and incoming (large to small r) solution, while we reserve Y_k^+ and Y_k^- to denote the solution vector on the exterior and interior of the k-the subdomain.

we can solve the above system for Φ_K^+ and Π_K^+ as

$$\Phi_K^+ = -\frac{1}{2}\Phi_K^- + \frac{\chi}{2g_{\theta\theta}}\Pi_K^- \tag{117a}$$

$$\Pi_K^+ = \frac{g_{\theta\theta}}{2\chi}\Phi_K^- - \frac{1}{2}\Pi_K^-. \tag{117b}$$

Though the point $r = 0$ is not a physical boundary of the domain Ω, it is a boundary of the computational domain in the sense that boundary conditions must be applied to the inner boundary of the subdomain D^1 in order to construct a stable scheme. Since it is clearly unphysical for new information to propagate into the computational domain from this coordinate boundary, we will apply Sommerfeld boundary conditions to this inner boundary in simulations in which there is not an inner excision surface present. In analogy to the above construction we construct the external solution Y_1^+ by solving the linear system determined by the constraints $X^-(Y_1^+) = X^-(Y_1^-)$ and $X^+(Y_1^+) = X^+(Y_1^-)$. This provides us with a solution Y_1^+ that has incoming (traveling from large to small r) characteristics whose component matter variables are given by

$$\Phi_1^+ = \frac{1}{2}\Phi_1^- + \frac{\chi}{2g_{\theta\theta}}\Pi_1^- \tag{118a}$$

$$\Pi_1^+ = \frac{g_{\theta\theta}}{2\chi}\Phi_1^- + \frac{1}{2}\Pi_1^-. \tag{118b}$$

4. Constructing Initial Data

Our primary goal is to model a localized wave pulse falling from far away into a black hole. In spherical symmetry this represents a collapsing spherical shell of scalar matter. To construct our pulse, note that the Schwarzschild solution is asymptotically flat, that is far away from the black hole spacetime approach Minkowski space. In this limit the massless Klein-Gordon equation reduces to the standard wave equation with velocity $c = 1$, and when further restricted to spherical symmetry it becomes the equation for a spherical wave

$$\partial_t^2(r\varphi) = \partial_r^2(r\varphi). \tag{119}$$

Let $\tilde{\varphi}(r,t) \equiv r\varphi(r,t)$. The above spherical wave equation has analytic solutions given by

$$\varphi(r,t) = \frac{1}{r}\tilde{\varphi}(r \pm t), \tag{120}$$

as may easily be verified, with the incoming solution is given by $\varphi(r,t) = \frac{1}{r}\tilde{\varphi}(r+t)$ [46]. It is therefore $\tilde{\varphi} = r\varphi$ that propagates in time with a constant amplitude and the analytic solution for φ in this $r \to \infty$ flat space limit should behave like $\varphi \sim 1/r$. The decay to zero amplitude at large r is also physically necessary for the pulse to have a finite energy as it become a sphere of infinite radius and the asymptotic behavior $\varphi(t, r \to \infty) = 0$ was assumed when we verified the form of the Lagrangian in Eq. (107). For simplicity we take $\tilde{\varphi}_0$ to be a Gaussian pulse centered at r_0 with amplitude A and width Δ. The initial data for the scalar field $\varphi_0 \equiv \tilde{\varphi}(t = 0, r; A, r_0, \Delta)$ is therefore given by

$$\tilde{\varphi}_0 = Ae^{-\left(\frac{r-r_0}{\Delta}\right)^2}, \qquad \varphi_0 = \frac{1}{r}Ae^{-\left(\frac{r-r_0}{\Delta}\right)^2}. \tag{121}$$

From this we can immediately calculate $\Phi_0 \equiv \Phi(t=0,r;A,r_0,\Delta)$ from the definition $\Phi = \partial_r\varphi$ and take

$$\Phi_0 = \frac{1}{r}\partial_r\tilde{\varphi}_0 - \frac{1}{r^2}\tilde{\varphi}_0 = \frac{2A(r_0-r)}{r\Delta^2}e^{-\left(\frac{r-r_0}{\Delta}\right)^2} - \frac{A}{r^2}e^{-\left(\frac{r-r_0}{\Delta}\right)^2}. \tag{122}$$

Since Π depends on $\partial_t\varphi$, our choice for $\Pi_0 \equiv \Pi(t=0,r;A,r_0,\Delta)$ will be used to enforce that the pulse is incoming. The incoming solution $\varphi(r,t) = \frac{1}{r}\tilde{\varphi}(r+t)$ satisfies $\partial_t\varphi = \frac{1}{r}\partial_t(r\varphi) = \frac{1}{r}\partial_r(r\varphi)$, and so our initial data should satisfy $\partial_t\varphi_0 = \Phi_0 + \frac{1}{r}\varphi_0$. This allows us to specify Π_0 according to its definition, Eq. (105a), as

$$\Pi_0 = \frac{\sqrt{g_{rr}}g_{\theta\theta}}{\alpha\chi^{3/2}}\left(\Phi_0(1-\beta^r) + \frac{\varphi_0}{r}\right) \tag{123}$$

To verify the accuracy of our dG scheme for solving the scalar field evolution equations, Eq. (106), we will consider simulations in Minkowski space, defined in spherical coordinates by the metric $ds^2 = -dt^2 + dr^2 + r^2d\Omega^2$. This specifies initial data for the evolved GBSSN fields given by

$$\begin{aligned} &g_{rr} = 1, \qquad g_{\theta\theta} = r^2, \qquad \chi = 1, \\ &K = 0, \qquad A_{rr} = 0, \qquad \Gamma^r = -2/r, \\ &\alpha = 1, \qquad \beta^r = 0, \qquad B^r = 0. \end{aligned} \tag{124}$$

In particular we have for this initial geometry $\Pi_0 = r^2\Phi_0 + r\varphi_0$.

The remainder of our simulations will use the Kerr-Schild initial data given in Eq. (94) to model the infall of our scalar field pulse into an un-charged, non-rotating black hole. Note that this choice of initial data actually violates the Hamiltonian and momentum GBSSN constraints since the Kerr-Schild data satisfies the vacuum constraints but the presence of the scalar field pulse dictates $\rho,\ j^r \neq 0$. We are therefore limited to situations in which the scalar field pulse can be considered as a perturbation of the black hole spacetime. As long as the initial amplitude A and width Δ are sufficiently small compared to the black hole mass M, the initial constraint violations will likewise be small and there will be no significant loss of accuracy so long as the violations do not grow in time or lead to numerical instabilities. Since these are analytic constraint violations in the data rather than numerical artifacts we do not expect them to shrink with increasing computational resolution and we will therefore not be able to measure the convergence of the scheme by monitoring the magnitude of the GBSSN constraints.

C. Simulation Results

1. Accuracy in Minkowski Space

In order to directly verify the accuracy of our scheme for solving the matter evolution equations, we begin by simulating the propagation of a wave pulse in Minkowski space and comparing our numerical pulse to the known analytic solution. Since Γ^r still diverges at $r=0$ (an artifact of using spherical coordinates), we place our inner boundary slightly away from the origin and take our domain Ω to be $r = [0.4, 300]$. The computational domain Ω_h is defined by splitting this into 7 subdomains of equal length covering $[0.4, 10]$ and 30

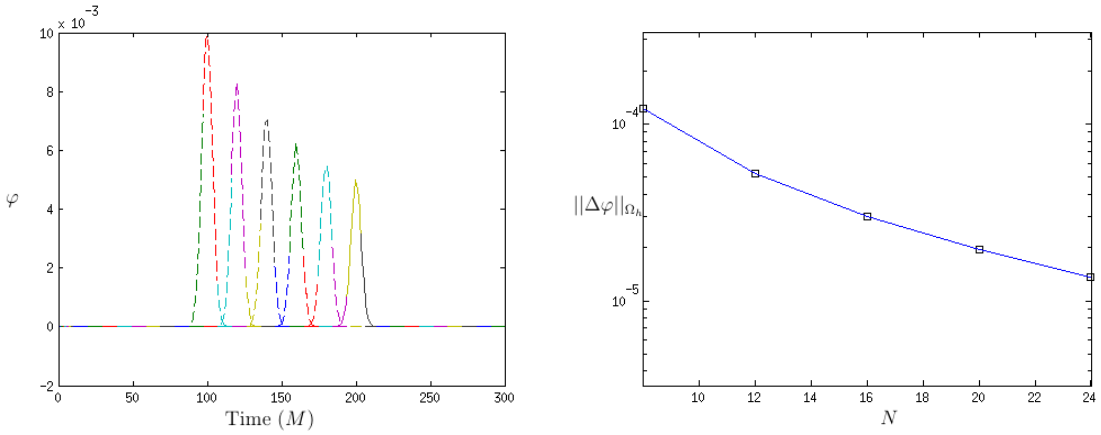

FIG. 8. Snapshots of the scalar pulse in Minkowski space and convergence. The left plot shows snapshots of a pulse with $A = 1$, $\Delta = 5$, $r_0 = 200$, and resolution $N = 10$ at various times. The solid line shows the initial pulse at $t = 0$, and the dashed lines show the pulse at $t = 20,\ 40,\ 60,\ 80,\ 100$. The left plot demonstrates the convergence of the scheme and shows log-scale $||\Delta\varphi||_{\Omega_h} \equiv ||\varphi - \varphi_{\text{exact}||_{\Omega_h}}$ with increasing N. These simulations used $A = 1$, $\Delta = 3$, and $r_0 = 150$ and the norm is measured at $t = 10$.

subdomains of equal length covering $[10, 300]$. We use a local Lax-Friendrichs flux with $C = 2$ for the numerical fluxes f^*_Φ and f^*_Π and as described above take $f^*_\varphi = 0$. We use the initial data for a purely incoming wave pulse given by Eqs. (121)-(123) and initialize the GBSSN variables to the Minkowski space values given in Eq. (124). Only the matter variables are evolved; the GBSSN variables are left constant with these values. We apply Sommerfeld boundary conditions at the inner and outer boundaries as given by Eq. (118) and Eq. (117) respectively. As before we use a fourth-order Runge Kutta method for time evolution with the timestep Δt chosen for stability. Since the matter evolution equations are linear there should be no aliasing error and we do not apply any filter to the system.

Simulations of this incoming wave pulse are robustly stable for all choices of A, Δ, and r_0 we have considered. Since there is no length scale other than the size of the domain there are no qualitative differences when A is varied over many orders of magnitude from 10^{-5} to 10^5. The presence of boundaries is not observed to introduce any complications, and upon reaching the inner boundary the incoming pulse reflects back in a stable manner. We can calculate the analytic solution φ_{exact} at later times according to $\varphi_{\text{exact}}(r, t) = \frac{1}{r}\tilde{\varphi}_0(t + r)$, where $\tilde{\varphi} = r\varphi$ as described above. Calculating the L_2 norm $||\varphi - \varphi_{\text{exact}}||_{\Omega_h}$ provides a direct measurement of the accuracy of these simulations. Fig. 8 shows that this error decays exponentially with increasing polynomial order N, so our scheme for solving the matter evolution equations possesses spectral convergence, as expected. Snapshots of $\varphi(x)$ at intervals of $t = 20$ from $t = 0$ to $t = 100$ are also shown in Fig. 8 and demonstrate that the scalar field has the desired qualitative behavior of an incoming Gaussian pulse whose width stays constant and amplitude grows with decreasing r.

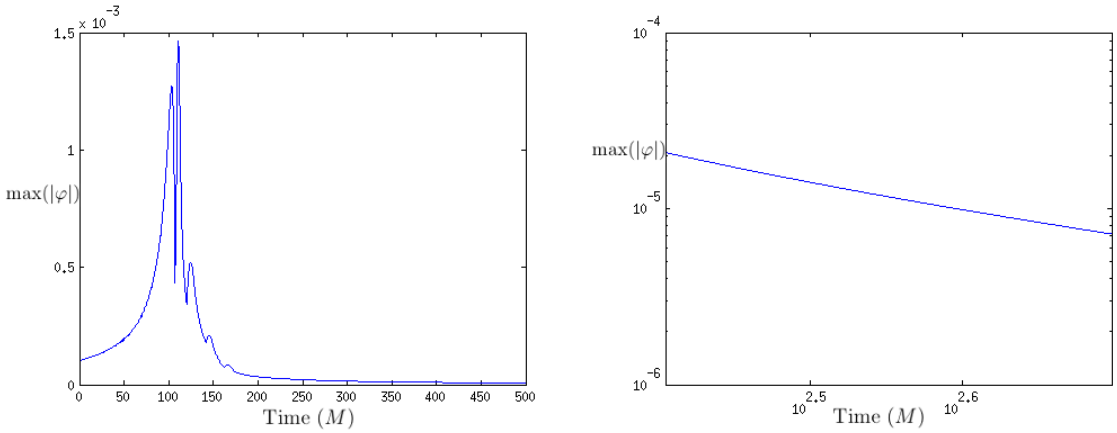

FIG. 9. Pulse amplitude during infall and power-law decay. The left plot shows $\max(|\varphi|)$ over the domain Ω during the full infall simulation from $t = 0$ to $t = 500$. The black hole is unit mass, $M = 1$, and the initial pulse has parameters $A = 10^{-2}M$, $\Delta = 3$, and $r_0 = 100$. The right plot shows a log-log plot of $\max(|\varphi|)$ over the domain for late times $t = 250$ to $t = 500$. The straight line in the log-log plot demonstrates a power-law decay.

2. Infall with a Kerr-Schild Black Hole

We now consider simulations with non-trivial gravitational coupling in which both the matter and GBSSN systems are evolved. We use the second order scheme to evolve the gravity sector and find that so long as the scalar field is small enough to be treated as a perturbation on the black hole spacetime no changes need to be make to the numerical setup used in Chapter V: we take $C = 2$, $\lambda = 0.1$, and $\eta = 50$ and consider a Schwarzschild black hole described in Kerr-Schild coordinates as before. To minimize any boundary effects we use a large computational domain Ω of $r = [0.4, 600]M$. With this domain choice the singularity of the black hole is managed through excision. The computational domain Ω_h is defined by splitting the region $[0.4, 10]M$ into 7 subdomains of equal length and the region $[10, 600]M$ into 60 subdomains of equal length. We use a local Lax-Friendrichs flux for all evolved fields, including the scalar field variables Φ and Π and take $f_\varphi = 0$ since $\Phi = \partial_r \varphi$ defines an auxiliary variable analogous to the Q sector of the abstract GBSSN system. As before we apply an exponential filter of strength $2s = 20$ to all fields except g_{rr} and $g_{\theta\theta}$, including the matter variables φ, Φ, and Π and choose the timestep Δt for stability. We use exact outer boundary conditions for the GBSSN fields and the Sommerfeld boundary conditions described above for Φ and Π.

Typical choices of initial data for the incoming pulse are $A = 10^{-2}M$, $\Delta = 3$, and $r_0 = 100$. This creates Hamiltonian constraint violations on the order of 10^{-8} near the pulse since the Kerr-Schild data satisfies the vacuum constraints. Constraint violations of this order propagate with the pulse and grow along with the amplitude as it moves inward, but there is no sign of uncontrolled growth in the constraints or changes in the qualitative shape of the GBSSN fields. With an initial amplitude of $A = 1M$ this is no longer the case: deformations of the metric are immediately visible and the constraint violations steadily grow until an instability develops just after $t = 100$. For $A = 10M$ an instability develops almost immediately. This is consistent with the idea that we can only model the scalar field

as a perturbation of the black hole geometry, and as long as the amplitude is taken to be sufficiently small relative to the black hole mass there is no sign of constraint growth or instability in simulations lasting for times in the hundreds of M.

The maximum absolute value (L_∞ norm) of the scalar field φ is shown as a function of time in Fig. 9. Qualitatively, the amplitude of the pulse increases as it moves inward, as in Minkowski space, until it reaches the black hole. The amplitude then falls off rapidly as it the pulse enters the horizon and travels off the inner boundary. After this initial infall, scalar matter is observed to radiate outward from the black hole. At late times the magnitude of this radiation decays as a power-law, as shown in Fig. 9. The precise decay rate is observed to depend on the details of the initial pulse. Observations of outgoing scalar radiation with a late-time power law decay are consistent with other numerical and analytic results, and in particular [30] calculates the precise exponent for the decay of each mode of a spherical harmonic decomposition of a scalar waveform. A straightforward application of this simulation code would be to monitor the amplitude of the radiated field at a fixed (areal) radius and compare the decay rate to the values predicted for different pulses. A further immediate application would be to consider more general initial pulses and study for example the absorption rates of different pulses as considered in finite difference simulations in [48]. More generally we hope that dG methods will soon be applied to more complicated and astrophysically interesting matter systems than the simple scalar field we have considered here.

VIII. CONCLUSION

Discontinuous Galerkin methods appear to be a promising technique for simulations in numerical relativity. After presenting a review of reformulating GR for initial value problems and the GBSSN system and a description of a dG scheme for solving the system and the turduckening technique for managing singular initial data describing black holes, we presented a number of new black hole simulations using dG methods that build upon the scheme constructed by Field et. al. in [23]. This previous work presented robustly stable and spectrally accurate second order dG simulations of a black hole in spherical symmetry that removed the singularity from the computational grid via excision, and in this thesis we showed that robust stability and spectral convergence were maintained when the interior of the black hole was included in the domain but the singularity was smoothed away using the turduckening technique. We further found that the initial constraint violations due to turduckening quickly decayed, as observed in the turduckened finite difference simulations of [14], and moreover that the rate of this decay increased with the smoothness of the stuffing transformation at the boundary of the turduckened region. At high resolution simulations using excision and turduckened were found to have similar levels of constraint violations once these violations in the initial data decayed.

We then presented a first order reduction of the GBSSN system and the results of dG simulations of this FOBSSN system recently published in [11]. Unlike the second order simulations that relied on using an analytic solution for outer boundary conditions, dG FOBSSN simulations were found to be stable and spectrally accurate with Sommerfeld boundary conditions enforced at the outer boundary. We discovered an ambiguity in turduckening the auxiliary fields in FOBSSN initial data were unable to construct stable simulations of FOBSSN using turduckening.

Finally, we considered dG simulations with dynamic matter fields coupled to the gravity

sector. For simplicity we considered the infall of a massless scalar field into a schwarzschild black hole. We presented a derivation of evolution equations for this scalar field in terms of our evolved GBSSN variables and constructed a spectrally accurate dG solver for the Klein-Gordon equation that we then incorporated into our second order black hole simulations with the appropriate gravitational coupling. The resulting simulations were found to be robustly stable so long as the amplitude of the initial incoming Gaussian pulse had an amplitude sufficiently small relative to the black hole mass that its gravitational effects could effectively be considered a perturbation on the black hole spacetime. We observed that after this incoming pulse fell into the black hole outgoing scalar radiation was emitted that at late times decayed according to a power-law.

It is our hope that this work can be expanded towards the construction of a general three-dimensional dG BSSN solver capable of efficiently simulating binary black hole collisions as well as non-vacuum simulations containing dynamic matter fields.

IX. ACKNOWLEDGMENTS

I would like to firstly thank my adviser Jan Hesthaven for all his support. I also owe a huge debt to Scott Field for his tireless help and email correspondence during and after his time at Brown. I would like to thank Stephen Lau for all his behind the scenes support on building the dG code. I would also like to thank Manuel Tiglio for all his help with the FOBSSN paper along with and everyone else who contributed to the paper. I want to thank Brown University and the UTRA program for supporting me on this research in summer 2011. Finally, I want to give a big thanks to all my friends and roommates who put up with me talking about turduckening for over a year now.

---

[1] Miguel Alcubierre, Bernd Bruegmann, Peter Diener, Michael Koppitz, Denis Pollney, et al. Gauge conditions for long term numerical black hole evolutions without excision. *Phys.Rev.*, D67:084023, 2003.

[2] Elspeth W. Allen, Elizabeth Buckmiller, Lior M. Burko, and Richard H. Price. Radiation tails and boundary conditions for black hole evolutions. *Phys.Rev.*, D70:044038, 2004.

[3] Douglas N. Arnold, Franco Brezzi, Bernardo Cockburn, and L. Donatella Marini. Unified analysis of discontinuous galerkin methods for elliptic problems. *SIAM J. Numer. Anal.*, 39(5):1749–1779, 2001.

[4] Richard L. Arnowitt, Stanley Deser, and Charles W. Misner. The Dynamics of general relativity. 1962. Gravitation: an introduction to current research, Louis Witten ed. (Wilew 1962), chapter 7, pp 227-265.

[5] Leor Barack. Late time dynamics of scalar perturbations outside black holes. 1. A Shell toy model. *Phys.Rev.*, D59:044016, 1999.

[6] Leor Barack. Late time dynamics of scalar perturbations outside black holes. 2. Schwarzschild geometry. *Phys.Rev.*, D59:044017, 1999.

[7] Thomas W. Baumgarte. Black Holes: from Speculations to Observations. *AIP Conf.Proc.*, 861:161–175, 2006.

[8] Thomas W. Baumgarte and Stuart L. Shapiro. On the numerical integration of Einstein's field equations. *Phys.Rev.*, D59:024007, 1999.

[9] Thomas W. Baumgarte and Stuart L. Shapiro. Numerical relativity and compact binaries. *Phys.Rept.*, 376:41–131, 2003.

[10] J. David Brown. Covariant formulations of BSSN and the standard gauge. *Phys.Rev.*, D79:104029, 2009.

[11] J. David Brown, Peter Diener, Scott E. Field, Jan S. Hesthaven, Frank Herrmann, et al. Numerical simulations with a first order BSSN formulation of Einstein's field equations. 2012.

[12] J.David Brown. Conformal invariance and the conformal-traceless decomposition of the gravitational field. *Phys.Rev.*, D71:104011, 2005.

[13] J.David Brown. BSSN in spherical symmetry. *Class.Quant.Grav.*, 25:205004, 2008.

[14] J.David Brown, Peter Diener, Olivier Sarbach, Erik Schnetter, and Manuel Tiglio. Turduckening black holes: An Analytical and computational study. *Phys.Rev.*, D79:044023, 2009.

[15] J.David Brown, Olivier Sarbach, Erik Schnetter, Manuel Tiglio, Peter Diener, et al. Excision without excision: The Relativistic turducken. *Phys.Rev.*, D76:081503, 2007.

[16] Lior M. Burko and Amos Ori. Late time evolution of nonlinear gravitational collapse. *Phys.Rev.*, D56:7820–7832, 1997.

[17] Gioel Calabrese, Jorge Pullin, Olivier Sarbach, and Manuel Tiglio. Convergence and stability in numerical relativity. *Phys.Rev.*, D66:041501, 2002.

[18] Sean M. Carroll. Spacetime and geometry: An introduction to general relativity. 2004.

[19] H.P. De Oliveira and I. Damiao Soares. Galerkin method in the gravitational collapse: A Dynamical system approach. *Phys.Rev.*, D65:064029, 2002.

[20] R. d'Inverno. Introducing Einstein's relativity. 1992.

[21] Manfredo P. do Carmo. *Riemannian Geometry*. Birkhäuser, Boston, MA, 1992.

[22] Scott E. Field. Applications of discontinuous galerkin methods to computational general relativity. *Brown University PhD Dissertation*, 2011.

[23] Scott E. Field, Jan S. Hesthaven, Stephen R. Lau, and Abdul H. Mroue. Discontinuous Galerkin method for the spherically reduced BSSN system with second-order operators. *Phys. Rev.*, D82:104051, 2010.

[24] J.A. Gonzalez and F.S. Guzman. Accretion of phantom scalar field into a black hole. *Phys.Rev.*, D79:121501, 2009.

[25] Eric Gourgoulhon. 3+1 formalism and bases of numerical relativity. 2007. Lecture notes.

[26] Carsten Gundlach. Critical phenomena in gravitational collapse. *Phys.Rept.*, 376:339–405, 2003.

[27] Carsten Gundlach and Jose M. Martin-Garcia. Symmetric hyperbolic form of systems of second order evolution equations subject to constraints. *Phys.Rev.*, D70:044031, 2004.

[28] Carsten Gundlach and Jose M. Martin-Garcia. Hyperbolicity of second-order in space systems of evolution equations. *Class.Quant.Grav.*, 23:S387–S404, 2006.

[29] Carsten Gundlach and Jose M. Martin-Garcia. Critical phenomena in gravitational collapse. *Living Rev.Rel.*, 10:5, 2007.

[30] Carsten Gundlach, Richard H. Price, and Jorge Pullin. Late time behavior of stellar collapse and explosions: 1. Linearized perturbations. *Phys.Rev.*, D49:883–889, 1994.

[31] J Hesthaven. Nodal high-order methods on unstructured grids i. time-domain solution of maxwells equations. *Journal of Computational Physics*, 181(1):186–221, 2002.

[32] J. S. Hesthaven and T. Wasburton. *Nodal Discontinuous Galerkin Methods Algorithms, Analysis, and Applications*. Springer, 2007.

[33] Russell A. Hulse. The discovery of the binary pulsar. *Rev. Mod. Phys.*, 66:699–710, Jul 1994.

[34] J. Kaplan, C. Ott, C. Muhlberger, M. Duez, F. Foucart, and M. Scheel. Simulations of Neutron-Star Binaries using the Spectral Einstein Code (SpEC). In *APS Meeting Abstracts*, page 14005, February 2010.

[35] Irving Kaplansky. *Linear Algebra and Geometry: Second Course*. Chelsea Pub Co, 1974.

[36] Paola Leaci. Searching for continuous gravitational wave signals using LIGO and Virgo detectors. *J.Phys.Conf.Ser.*, 354:012010, 2012.

[37] J. M. Lee. Riemannian Manifolds: An Introduction to Curvature. 1997.

[38] J.M. Lee. *Introduction to Smooth Manifolds*. 2005.

[39] R.L. Marsa and M.W. Choptuik. Black hole scalar field interactions in spherical symmetry. *Phys.Rev.*, D54:4929–4943, 1996.

[40] Charles W. Misner, K.S. Thorne, and J.A. Wheeler. Gravitation. 1974.

[41] Dario Nunez and Olivier Sarbach. Boundary conditions for the Baumgarte-Shapiro-Shibata-Nakamura formulation of Einstein's field equations. *Phys.Rev.*, D81:044011, 2010.

[42] Harald P. Pfeiffer. Numerical simulations of compact object binaries. 2012.

[43] David Radice and Luciano Rezzolla. Discontinuous Galerkin methods for general-relativistic hydrodynamics: formulation and application to spherically symmetric spacetimes. *Phys.Rev.*, D84:024010, 2011.

[44] Bernard Schutz. *Geometrical Methods of Mathematical Physics*. 1980.

[45] Bernard F. Schutz. A First Course In General Relativity. Cambridge, Uk: Univ. Pr. (1985) 376p.

[46] W.A. Strauss. *Partial Differential Equations: An Introduction*. Wiley, 1992.

[47] Slava G. Turyshev. Experimental Tests of General Relativity. *Ann.Rev.Nucl.Part.Sci.*, 58:207–248, 2008.

[48] L. Arturo Urena-Lopez and Lizbeth M. Fernandez. Black holes and the absorption rate of cosmological scalar fields. *Phys.Rev.*, D84:044052, 2011. 5 pages, 5 color figures, uses REVTex.